

CERN-PH-EP-2012-069

12 October 2012

Suppression of high transverse momentum D mesons in central Pb–Pb collisions at $\sqrt{s_{\text{NN}}} = 2.76$ TeV

ALICE Collaboration*

Abstract

The production of the prompt charm mesons D^0 , D^+ , D^{*+} , and their antiparticles, was measured with the ALICE detector in Pb–Pb collisions at the LHC, at a centre-of-mass energy $\sqrt{s_{\text{NN}}} = 2.76$ TeV per nucleon–nucleon collision. The p_t -differential production yields in the range $2 < p_t < 16$ GeV/ c at central rapidity, $|y| < 0.5$, were used to calculate the nuclear modification factor R_{AA} with respect to a proton–proton reference obtained from the cross section measured at $\sqrt{s} = 7$ TeV and scaled to $\sqrt{s} = 2.76$ TeV. For the three meson species, R_{AA} shows a suppression by a factor 3–4, for transverse momenta larger than 5 GeV/ c in the 20% most central collisions. The suppression is reduced for peripheral collisions.

arXiv:1203.2160v5 [nucl-ex] 5 Apr 2017

*See Appendix A for the list of collaboration members

1 Introduction

A high-density colour-deconfined state of strongly-interacting matter is expected to be formed in high-energy collisions of heavy nuclei. According to calculations of Quantum Chromodynamics (QCD) on the lattice, under the conditions of high energy density and temperature reached in these collisions, a phase transition to a Quark-Gluon Plasma (QGP) occurs. In such conditions, the confinement of quarks and gluons into hadrons vanishes, and chiral symmetry is restored (see e.g. [1–3]). Heavy-flavour hadrons, containing charm and beauty, are effective probes of the conditions of the medium formed in nucleus–nucleus collisions at high energy. Hard partons, including gluons, light-flavour quarks, and heavy quarks, are produced at the initial stage of the collision in high-virtuality scattering processes. They interact with the medium, and are expected to be sensitive to its energy density, through the mechanism of parton energy loss. This QCD energy loss is expected to occur via both inelastic (medium-induced gluon radiation, or radiative energy loss) [4, 5] and elastic (collisional energy loss) [6] processes. In QCD, quarks have a smaller colour coupling factor with respect to gluons, so that the energy loss for quarks is expected to be smaller than for gluons. In addition, the ‘dead-cone effect’ should reduce small-angle gluon radiation for heavy quarks with moderate energy-over-mass values [7–11], thus further attenuating the effect of the medium. Instead, other mechanisms, such as in-medium hadron formation and dissociation [12, 13], would determine a stronger effect on heavy-flavour hadrons, characterized by smaller formation times than light-flavour hadrons. Finally, low-momentum heavy quarks may be to some extent thermalized in the hot and dense system through rescatterings and in-medium resonant interactions [14].

One of the observables that are sensitive to the interaction of hard partons with the medium is the nuclear modification factor R_{AA} . This quantity is defined as the ratio of particle production measured in nucleus–nucleus (AA) to that expected from the proton–proton (pp) spectrum scaled by the average number $\langle N_{\text{coll}} \rangle$ of binary nucleon–nucleon collisions occurring in the nucleus–nucleus collision. Using the nuclear overlap function, which is defined as the convolution of the nuclear density profiles of the colliding ions in the Glauber model [15], the nuclear modification factor of the transverse momentum (p_t) distribution can be expressed as:

$$R_{\text{AA}}(p_t) = \frac{1}{\langle T_{\text{AA}} \rangle} \cdot \frac{dN_{\text{AA}}/dp_t}{d\sigma_{\text{pp}}/dp_t}, \quad (1)$$

where the AA spectrum corresponds to a given collision-centrality class and $\langle T_{\text{AA}} \rangle$ is the average nuclear overlap function for that centrality class and is proportional to $\langle N_{\text{coll}} \rangle$. In-medium energy loss determines a suppression, $R_{\text{AA}} < 1$, of hadrons at moderate-to-high transverse momentum ($p_t \gtrsim 2$ GeV/ c). Given the aforementioned properties of parton energy loss, in the range $p_t \lesssim 10$ GeV/ c where the heavy-quark masses are not negligible with respect to their momenta, an increase of the R_{AA} value (i.e. a smaller suppression) is expected when going from the mostly gluon-originated light-flavour hadrons (e.g. pions) to D and B mesons (see e.g. [10, 16]): $R_{\text{AA}}^\pi < R_{\text{AA}}^{\text{D}} < R_{\text{AA}}^{\text{B}}$. The measurement and comparison of these different medium probes should provide a unique test of the colour-charge and mass dependence of parton energy loss.

Experiments at the Relativistic Heavy Ion Collider (RHIC) measured a strong suppression, by a factor 4–5 at $p_t > 5$ GeV/ c , for light-flavour hadrons in central Au–Au collisions at $\sqrt{s_{\text{NN}}} = 200$ GeV [17]. An even stronger suppression—up to a factor 7 at $p_t \approx 6$ –8 GeV/ c —was observed in central Pb–Pb collisions at $\sqrt{s_{\text{NN}}} = 2.76$ TeV at the Large Hadron Collider (LHC) [18–20]. At RHIC, the suppression of heavy-flavour hadrons, measured indirectly from their inclusive decay electrons [21, 22], was found to be compatible with that of pions and generally stronger than most expectations based on radiative energy loss [23, 24]. At the LHC, a measurement by the CMS Collaboration indicates a strong suppression, by a factor about 3, in the nuclear modification factor of non-prompt J/ψ particles from B meson decays [25].

We present the first measurement of the nuclear modification factor for D^0 , D^+ , D^{*+} mesons, and their

antiparticles, in Pb–Pb collisions at $\sqrt{s_{NN}} = 2.76$ TeV, carried out using the ALICE detector. The experimental apparatus [26] is briefly presented in Section 2, where the Pb–Pb data sample used for this analysis is also described. The D meson signals are extracted using a selection based on displaced decay vertex reconstruction and particle identification of the decay products, as presented in Section 3. The corrections applied to obtain the p_t -differential production yields, and the estimation of the systematic uncertainties are described in Sections 4 and 6, respectively. The production of D mesons was measured in proton–proton collisions at $\sqrt{s} = 7$ TeV and compared to perturbative QCD (pQCD) predictions [27]. The reference for the R_{AA} measurements was obtained by scaling these results to the Pb–Pb energy via a pQCD-driven approach and was validated by comparing to data from a limited-statistics pp sample at this energy [28]. This is discussed in Section 5. The results on the D^0 , D^+ , and D^{*+} nuclear modification factors as a function of transverse momentum and collision centrality are presented in Section 7. The results are compared to the charged particle R_{AA} measured with the ALICE detector [19], to the non-prompt J/ψ results by the CMS Collaboration [25], and to model predictions.

2 Experimental apparatus, data sample, event reconstruction and selection

The ALICE detector, described in detail in [26], consists of a central barrel composed of various detectors for particle reconstruction at midrapidity, a forward muon spectrometer, and a set of forward detectors for triggering and event characterization. In the following, the subsystems that are utilized in the D meson analysis will be briefly described. In particular, the Inner Tracking System (ITS), the Time Projection Chamber (TPC), and the Time Of Flight (TOF) detector provide charged particle reconstruction and identification in the central pseudo-rapidity region ($|\eta| < 0.9$). They are embedded in a 0.5 T magnetic field parallel to the LHC beam direction (z -axis in the ALICE reference frame). The VZERO detector and the Zero Degree Calorimeters (ZDC) are used for triggering and event selection, and the T0 detector to measure the start time (event time-zero) of the collision.

The data from Pb–Pb collisions at centre-of-mass energy $\sqrt{s_{NN}} = 2.76$ TeV used for this analysis were recorded in November and December 2010 during the first run with heavy-ions at the LHC. The events were collected with an interaction trigger based on the information of the Silicon Pixel Detector (SPD) and the VZERO detector. The SPD is the innermost part of the ITS. It consists of two cylindrical layers of silicon pixel detectors located at radial positions of 3.9 and 7.6 cm from the beam line, covering the pseudo-rapidity ranges $|\eta| < 2.0$ and $|\eta| < 1.4$, respectively. The SPD contributes to the minimum-bias trigger if hits are detected on at least two different chips (each covering a detector area of 1.28×1.41 cm²) on the outer layer. The VZERO detector is composed of two arrays of scintillator tiles covering the full azimuth in the pseudo-rapidity regions $2.8 < \eta < 5.1$ (VZERO-A) and $-3.7 < \eta < -1.7$ (VZERO-C). The events used in this analysis were collected with two different interaction trigger configurations: in the first part of the data taking period, signals in two out of the three triggering detectors (SPD, VZERO-A, VZERO-C) were required, while in the second part a coincidence between the VZERO-A and VZERO-C detectors was used. Events were further selected offline to remove background coming from parasitic beam interactions on the basis of the timing information provided by the VZERO and the neutron ZDC detectors (two calorimeters located at $z \approx \pm 114$ m from the interaction point). It was verified that the timing information from the ZDCs was available in all the hadronic interactions that passed the trigger condition. The luminous region had an r.m.s. width of about 6 cm in the longitudinal direction and 50–60 μ m in the transverse direction. These values were stable during the entire data taking period. Only events with a vertex found within ± 10 cm from the centre of the detector along the beam line were considered for the D meson signal extraction.

Collisions were classified according to their centrality, defined in terms of percentiles of the hadronic Pb–Pb cross section and determined from the distribution of the summed amplitudes in the VZERO scintillator tiles. To obtain the total hadronic cross section, this distribution was fitted using the Glauber model for the geometrical description of the nuclear collision [15] complemented by a two-component

Table 1: Average values of the number of participating nucleons, and of the nuclear overlap function for the considered centrality classes, expressed as percentiles of the hadronic cross section. The values were obtained with a Monte Carlo implementation of the Glauber model assuming an inelastic nucleon–nucleon cross section of 64 mb [30].

Centrality class	$\langle N_{\text{part}} \rangle$	$\langle T_{\text{AA}} \rangle$ (mb $^{-1}$)
0–20%	308 ± 3	18.93 ± 0.74
40–80%	46 ± 2	1.20 ± 0.07
0–10%	357 ± 4	23.48 ± 0.97
10–20%	261 ± 4	14.43 ± 0.57
20–40%	157 ± 3	6.85 ± 0.28
40–60%	69 ± 2	2.00 ± 0.11
60–80%	23 ± 1	0.42 ± 0.03

model for particle production [29,30]. The fit was performed in a range of measured VZERO amplitudes where the trigger is fully efficient for hadronic interactions and the contamination by electromagnetic processes is negligible [30]. This range corresponds to $90 \pm 1\%$ of the total hadronic cross section. The nuclear modification factor R_{AA} was measured for D^0 , D^+ , and D^{*+} mesons as a function of transverse momentum for the centrality classes 0–20% and 40–80%. In order to study in more detail its centrality dependence, R_{AA} was also evaluated, for wide p_t intervals, in narrower centrality classes: 0–10%, 10–20%, 20–40%, 40–60%, and 60–80%. Table 1 shows the average values of the number of participating nucleons $\langle N_{\text{part}} \rangle$, and of the nuclear overlap function $\langle T_{\text{AA}} \rangle$ in these centrality classes. In the centrality range considered in this analysis, 0–80%, and for both the configurations of the interaction trigger described above, the trigger and event selection are fully efficient for hadronic interactions, and the contamination by electromagnetic processes is negligible.

In total, 13×10^6 Pb–Pb collisions with centrality in the range 0–80% passed the selection criteria described above and were used in the analysis. The corresponding integrated luminosity is $L_{\text{int}} = 2.12 \pm 0.07 \mu\text{b}^{-1}$.

The trajectories of the D meson decay particles were reconstructed from their hits in the TPC and in the ITS. The TPC [31] provides track reconstruction with up to 159 three-dimensional space points per track in a cylindrical active volume that covers the region $85 < r < 247$ cm and $-250 < z < +250$ cm in the radial and longitudinal directions, respectively. The ITS [32] consists of six cylindrical layers of silicon detectors with radii in the range between 3.9 cm and 43.0 cm. Around the two innermost layers equipped with pixel detectors (SPD, described above), Silicon Drift Detectors (SDD) are used in the two intermediate layers, while the two outermost layers are made of double-sided Silicon Strip Detectors (SSD). The alignment of the ITS sensor modules, which is crucial to achieve the high space point resolution needed in heavy flavour analysis, was performed using survey information, cosmic-ray tracks, and pp data, with the methods described in [32]. For the residual misalignment along the $r\phi$ coordinate, an r.m.s. of about $8 \mu\text{m}$ for SPD and $15 \mu\text{m}$ for SSD modules was estimated [32,33]. For SDD, with the calibration level reached on the 2010 data sample, the space point resolution along $r\phi$ is $\approx 60 \mu\text{m}$ for those modules that do not suffer from significant drift field non-uniformities. The residual misalignment is included in an effective way in the detector simulation by randomly displacing the ITS modules with respect to their ideal positions according to the estimated precision of the alignment.

The primary vertex position and covariance matrix were determined from the tracks reconstructed in the TPC and ITS by using an analytic χ^2 minimization method, applied after approximating the tracks to straight lines in the vicinity of their common origin. The same algorithm was used for the reconstruction of the decay vertices of D^0 and D^+ candidates. The high spatial resolution of the reconstructed hits, together with the low material budget (on average 7.7% of a radiation length for the ITS at $\eta = 0$) and the small distance of the innermost layer from the beam vacuum tube, allows for the measurement of the

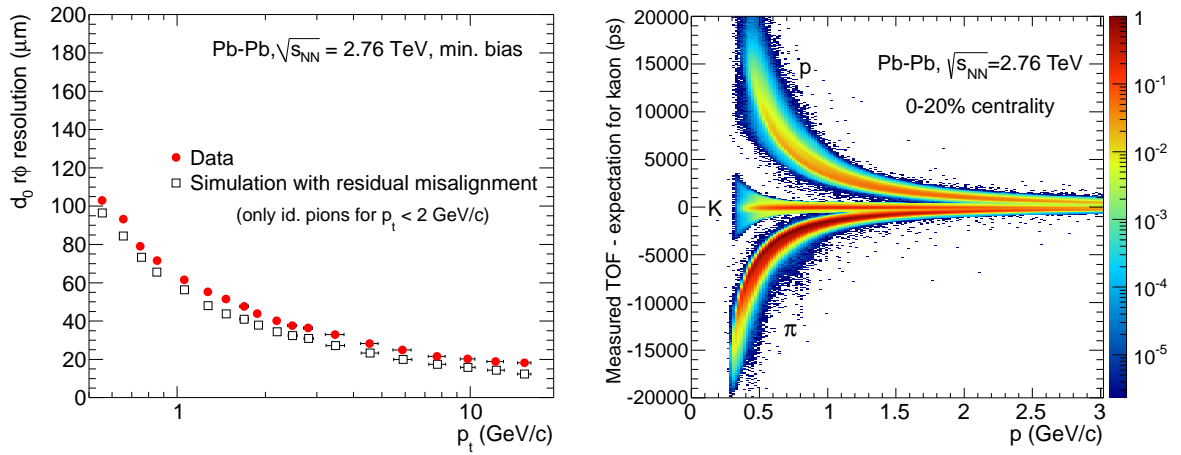


Figure 1: Left: track impact parameter resolution in the transverse plane as a function of p_t in Pb–Pb collisions. For $p_t < 2$ GeV/ c , pion identification by the TPC or TOF detectors is required; the results for data and simulation are shown. The simulation includes the effect of the residual geometrical misalignment of the sensor modules of the Inner Tracking System (see text for details). Right (colour online): difference between the measured time-of-flight and that expected under the kaon hypothesis as a function of track momentum for the 20% most central Pb–Pb collisions.

track impact parameter in the transverse plane (d_0), i.e. the distance of closest approach of the track to the primary vertex along $r\phi$, with a resolution better than $65 \mu\text{m}$ for transverse momenta $p_t > 1$ GeV/ c . The impact parameter resolution σ_{d_0} is shown in the left-hand panel of Fig. 1 as a function of p_t , for data and simulation, for charged hadron tracks selected with the same criteria used in the D meson analysis. The applied track quality cuts were based on the request of having at least 70 associated space points (out of a maximum of 159) in the TPC with a χ^2 per degree-of-freedom of the momentum fit lower than 2, and at least 2 associated hits in the ITS, out of which at least one has to be in the silicon pixel layers. Only tracks with transverse momentum $p_t > 0.5$ GeV/ c (0.7 for the 20% most central collisions) and $|\eta| < 0.8$ were used for the D meson analysis and are displayed in Fig. 1 (left). For $p_t < 2$ GeV/ c , only particles identified as pions were selected, as explained in the next paragraph. The impact parameter resolution is better than for pp collisions [27], e.g. by $\approx 10 \mu\text{m}$ at $p_t = 1$ GeV/ c , since, in the Pb–Pb case, the primary vertex is reconstructed using a larger number of tracks, hence with better precision. Indeed, the resolution on the transverse coordinates of the primary vertex is about $5 \mu\text{m}$ in central Pb–Pb collisions, while it is up to $40 \mu\text{m}$ in pp [27]. The systematic effect on the D meson analysis of the small difference in resolution ($5 \mu\text{m}$) between data and simulation will be discussed in Section 6. The resolution on the transverse momentum of tracks reconstructed in the TPC and in the ITS, and passing the quality selection criteria described above, was measured to be about 1% at $p_t = 1$ GeV/ c and about 2% at $p_t = 10$ GeV/ c .

The particle identification (PID) capabilities are provided by the measurement of the specific energy loss dE/dx in the TPC and of the time-of-flight in the TOF detector. The dE/dx samples measured by the TPC are reduced, by means of a truncated mean, to a Gaussian distribution with a resolution of $\sigma_{dE/dx}/(dE/dx) \approx 6\%$ which is slightly dependent on track quality and detector occupancy. The TOF detector [34] is positioned at 370–399 cm from the beam axis and covers the full azimuth and the pseudorapidity range $|\eta| < 0.9$. In Pb–Pb collisions, in the centrality range 0–70%, the overall time-of-flight resolution was measured to be about 90 ps for pions with a momentum of 1 GeV/ c . This value includes the detector intrinsic resolution, the electronics and calibration contribution, the uncertainty on the start time of the event, and the tracking and momentum resolution. The start time of the event is measured by the T0 detector, made of two arrays of Cherenkov counters located on either side of the interaction point

and covering the pseudorapidity ranges $-3.28 < \eta < -2.97$ and $4.61 < \eta < 4.92$, respectively. For the events in which the T0 signal is not present, the start time is estimated using the particle arrival times at the TOF. In the centrality class 70–80%, the TOF resolution slightly worsens due to the increasing uncertainty on the start time determination, while still remaining below 100 ps.

In the right-hand panel of Fig. 1, the difference between the measured time-of-flight and that expected under the kaon hypothesis is shown as a function of the track momentum for Pb–Pb collisions in the centrality range 0–20%, illustrating the separation between pions, kaons and protons. The expected time-of-flight is calculated for the given mass hypothesis from the total integrated path length and the measured momentum of the track. A compatibility cut with the PID response from the TPC was used in order to decrease the contamination from tracks with wrong hit association in the TOF detector. The bands corresponding to particles identified as pions (upper band), kaons (middle) and protons (lower band) are separated up to $p \approx 2$ GeV/ c , corresponding to the momentum range in which the TOF PID is used in this analysis.

3 D meson reconstruction and selection

The D^0 , D^+ , and D^{*+} mesons and their antiparticles were reconstructed in the central rapidity region from their charged hadronic decay channels $D^0 \rightarrow K^- \pi^+$ (with branching ratio, BR, of $3.87 \pm 0.05\%$ and mean proper decay length $c\tau \approx 123$ μm), $D^+ \rightarrow K^- \pi^+ \pi^+$ (BR of $9.13 \pm 0.19\%$, $c\tau \approx 312$ μm), and $D^{*+} \rightarrow D^0 \pi^+$ (strong decay with BR of $67.7 \pm 0.5\%$) [35]. The D meson yields were extracted from an invariant mass analysis of fully reconstructed decay topologies displaced with respect to the primary vertex, using the same procedure as for pp collisions [27].

D^0 and D^+ candidates were defined from pairs and triplets of tracks with proper charge sign combination and selected by requiring at least 70 associated space points in the TPC, with $\chi^2/\text{ndf} < 2$, and at least 2 associated hits in the ITS, out of which at least one in the SPD. A fiducial acceptance cut $|\eta| < 0.8$ was applied as well, along with a transverse momentum threshold $p_t > 0.5$ GeV/ c (0.7 for the 20% most central collisions), aimed at reducing the large combinatorial background.

D^{*+} candidates were obtained by combining the D^0 candidates with tracks selected with transverse momentum $p_t > 0.2$ GeV/ c in the centrality range 0–20% and $p_t > 0.1$ GeV/ c in 20–80%. The momentum of the pion from the D^{*+} decay is typically low, because of the small mass difference between the D^{*+} and D^0 mesons. In order to reduce the combinatorics, these tracks were selected requiring at least 3 associated ITS hits (4 in the 0–20% centrality class), in addition to the same TPC quality selection as that used for the D^0 and D^+ decay tracks. In the centrality class 40–80%, also tracks reconstructed only in the ITS, with at least 3 hits, were used to enhance the D^{*+} signal at low p_t .

The selection of the D^0 and D^+ decays was based on the reconstruction of secondary vertex topologies, with a separation of a few hundred microns from the interaction point. In the case of the D^{*+} decay, the secondary vertex topology of the produced D^0 was reconstructed. The selection is essentially the same as that used for the pp case [27] and exploits the separation between the secondary and primary vertices (decay length) and the pointing of the reconstructed meson momentum to the primary vertex. The pointing condition is applied by requiring a small value for the angle θ_{pointing} between the directions of the reconstructed momentum of the candidate and of its flight line, defined by the positions of the primary and secondary vertices. In order to cope with the much larger combinatorial background and to exploit the better resolution on the reconstructed primary vertex position, the cuts were in general tightened with respect to the pp case. Two additional cuts, on the projections of the pointing angle and of the decay length in the transverse plane ($\theta_{\text{pointing}}^{\text{xy}}$ and L^{xy}), were introduced to further suppress the combinatorial background.

The cuts were defined so as to have large statistical significance of the signal and to keep the selection

efficiency as high as possible. This latter requirement was dictated also by the fact that too tight cuts result in an increased contribution to the raw yield from feed-down D mesons originating from decays of B mesons. It was also checked that background fluctuations were not causing a distortion in the signal line shape by verifying that the D meson mass and its resolution were in agreement with the PDG value and the simulation results, respectively. The resulting cut values depend on the D meson p_t and on the centrality of the event. They lead to a selection efficiency that increases with increasing p_t and decreases from peripheral to central collisions: looser cuts could be used for peripheral events, where the combinatorial background is lower. The cut values quoted in the following refer to the tightest selections in the lower p_t intervals for the 0–20% centrality class.

The PID selection relies on the pion and kaon identification by the TPC and TOF detectors. Cuts at $\pm 3\sigma$ around the expected mean energy deposit dE/dx and time-of-flight were used. This selection provides a strong reduction, by a factor of about 3, of the combinatorial background in the low- p_t region, while preserving most of the signal ($\approx 95\%$ according to simulations, as detailed in the next Section). In the D^{*+} case, a tighter PID cut at 2σ on the TPC dE/dx was applied to the D^0 decay products in the centrality class 0–20%, in order to cope with the large combinatorial background.

With the track selection described above, the acceptance in rapidity for D mesons drops steeply to zero for $|y| \gtrsim 0.5$ at low p_t and $|y| \gtrsim 0.8$ for $p_t \gtrsim 5$ GeV/ c . A p_t dependent fiducial acceptance cut was therefore applied on the D meson rapidity, $|y| < y_{\text{fid}}(p_t)$, with $y_{\text{fid}}(p_t)$ increasing from 0.5 to 0.8 in $0 < p_t < 5$ GeV/ c according to a second order polynomial function and taking a constant value of 0.8 for $p_t > 5$ GeV/ c .

For D^0 mesons, the two decay tracks were selected requiring a significance of the impact parameter with respect to the event primary vertex $|d_0|/\sigma_{d_0} > 0.5$ and a maximum distance of closest approach between each other of $250 \mu\text{m}$. The minimum decay length was set at $100 \mu\text{m}$. Furthermore, the cuts $d_0^\pi \times d_0^K < -45000 \mu\text{m}^2$ on the product of the decay track impact parameters and $L^{xy}/\sigma_{L^{xy}} > 7$ on the significance of the projection of the decay length in the transverse plane were applied. A selection on the angle θ^* between the kaon momentum in the D^0 rest frame and the boost direction was used to reduce the contamination of background candidates that do not represent real two-body decays and typically have large values of $|\cos \theta^*|$. The applied cut was $|\cos \theta^*| < 0.8$. The pointing of the D^0 momentum to the primary vertex was imposed via the cuts $\cos \theta_{\text{pointing}} > 0.95$ and $\cos \theta_{\text{pointing}}^{xy} > 0.998$.

For D^+ mesons, a decay length of at least 1.9 mm was required. It should be noted that D^+ mesons in the 0–20% centrality class are reconstructed only for $p_t > 6$ GeV/ c , where the Lorentz dilation of the D^+ lifetime allows for a tight cut on the decay length. Further requirements to reduce the combinatorial background were $\cos \theta_{\text{pointing}} > 0.995$, $\cos \theta_{\text{pointing}}^{xy} > 0.997$, $L^{xy}/\sigma_{L^{xy}} > 12$, and $\sum d_0^2 > (300 \mu\text{m})^2$ (sum of the squared impact parameters of the three decay tracks). The D^+ cuts are in general tighter than the D^0 ones because of the larger combinatorial background.

In the D^{*+} analysis, the selection of the decay D^0 was similar to that used for the D^0 analysis, with a tighter cut on the pointing angle, $\cos \theta_{\text{pointing}} > 0.99$. The decay pion was selected with the track quality cuts described above and requiring a minimum p_t that varied in the range 0.1–1 GeV/ c depending on the D^{*+} momentum and event centrality. In the 0–20% centrality class and for D^{*+} transverse momentum below 6 GeV/ c , a 3σ compatibility cut with respect to the pion expectation values was applied to the measured dE/dx and time-of-flight.

Figure 2 shows the invariant mass distributions of the selected D^0 , D^+ , and D^{*+} candidates in some of the p_t intervals used in the analysis, for the 0–20% centrality class. The D^0 and D^+ yields were extracted by fitting the distributions with a function composed of a Gaussian for the signal and an exponential term that describes the background shape. The D^{*+} background was described with a threshold function multiplied by an exponential [27]. The centroids of the Gaussians were found to be compatible with the PDG masses of the D mesons [35], and their widths to be well reproduced in the simulation. The

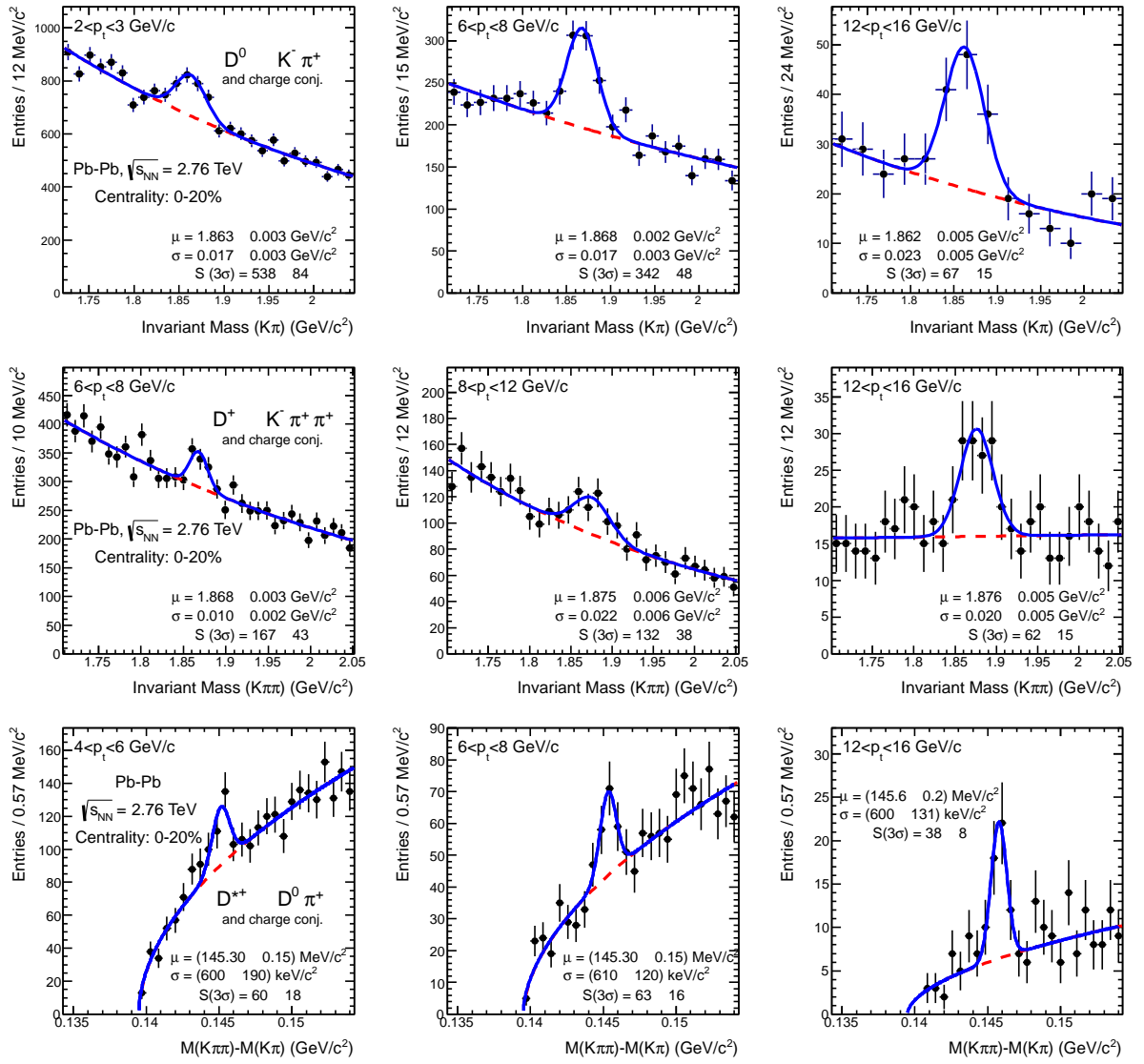


Figure 2: Invariant mass distributions for D^0 (upper panels), D^+ (central panels), and D^{*+} (lower panels) candidates and their charge conjugates in selected p_t intervals for 3.2×10^6 0–20% central Pb–Pb collisions. The curves show the fit functions described in the text. The values of mean (μ) and width (σ) of the signal peak are reported in the plots together with the raw signal yield. The uncertainties on the signal yields reported in the figures are statistical only.

signal yields (sum of particle and antiparticle) are reported in Table 2 for the p_t intervals considered in the analysis, for the centrality classes 0–20% and 40–80%.

4 Corrections

The D meson raw yields extracted from the fits to the invariant mass distributions were corrected to obtain the production yields for primary (i.e. not coming from weak decays of B mesons) D^0 , D^+ , and D^{*+} . The contribution of secondary D mesons from B decays, which is of the order of 15% as explained in the following, was estimated using pQCD predictions for B production and Monte Carlo simulations. The D mesons remaining after the subtraction of the B feed-down contribution are those produced at the interaction vertex, and they will be referred to as ‘prompt’ in the following.

Table 2: Measured raw yields for D^0 , D^+ , and D^{*+} mesons and their antiparticles in the transverse momentum intervals considered for the 0–20% and 40–80% centrality classes. The systematic uncertainty estimation is described in Section 6.

p_t interval (GeV/c)	$N^{\text{raw}} \pm \text{stat.} \pm \text{syst.}$					
	0–20% centrality			40–80% centrality		
	$D^0 + \bar{D}^0$	$D^+ + D^-$	$D^{*+} + D^{*-}$	$D^0 + \bar{D}^0$	$D^+ + D^-$	$D^{*+} + D^{*-}$
2–3	$538 \pm 84 \pm 43$	–	–	$231 \pm 31 \pm 12$	–	$82 \pm 21 \pm 12$
3–4	$774 \pm 108 \pm 46$	–	–	$241 \pm 32 \pm 12$	$58 \pm 19 \pm 9$	$82 \pm 21 \pm 12$
4–5	$583 \pm 79 \pm 35$	–	$60 \pm 18 \pm 12$	$176 \pm 20 \pm 9$	$114 \pm 22 \pm 6$	$36 \pm 7 \pm 5$
5–6	$318 \pm 67 \pm 19$	–		$87 \pm 13 \pm 4$		$29 \pm 9 \pm 3$
6–8	$342 \pm 48 \pm 21$	$167 \pm 43 \pm 33$	$63 \pm 16 \pm 6$	$113 \pm 14 \pm 6$	$130 \pm 34 \pm 20$	$47 \pm 13 \pm 5$
8–12	$327 \pm 41 \pm 20$	$132 \pm 38 \pm 20$	$55 \pm 12 \pm 6$	$107 \pm 15 \pm 6$	$119 \pm 26 \pm 18$	$57 \pm 11 \pm 6$
12–16	$67 \pm 15 \pm 7$	$62 \pm 15 \pm 6$	$38 \pm 8 \pm 4$	$41 \pm 9 \pm 2$	–	$23 \pm 6 \pm 2$

The prompt D meson production yields were calculated starting from the raw yields (N^{raw} , reported in the previous section) divided by a factor of two to evaluate the charge (particle and antiparticle) averaged yields. These were corrected for the B meson decay feed-down contribution (i.e. multiplied by the prompt fraction f_{prompt}), and divided by the acceptance-times-efficiency for prompt D mesons, $(\text{Acc} \times \varepsilon)_{\text{prompt}}$. They were normalized according to the decay channel branching ratio (BR), p_t interval width (Δp_t), rapidity coverage (Δy), and the number of events analyzed (N_{evt}). As an illustration, the D^+ yields were computed as:

$$\left. \frac{dN^{D^+}}{dp_t} \right|_{|y| < 0.5} = \frac{1}{\Delta y \Delta p_t} \frac{f_{\text{prompt}}(p_t) \cdot \frac{1}{2} N^{D^{\pm \text{raw}}}(p_t) \Big|_{|y| < y_{\text{fid}}}}{(\text{Acc} \times \varepsilon)_{\text{prompt}}(p_t) \cdot \text{BR} \cdot N_{\text{evt}}}. \quad (2)$$

As mentioned in Section 3, the D meson yields were measured in a rapidity range varying from $|y| < 0.5$ at low p_t to $|y| < 0.8$ at high p_t . The rapidity acceptance correction factor $\Delta y = 2y_{\text{fid}}$ assumes a uniform rapidity distribution for D mesons in the measured y range. This assumption was checked to the 1% level [27] with PYTHIA [36] pp simulations with the Perugia-0 tuning [37].

The acceptance-times-efficiency corrections $\text{Acc} \times \varepsilon$ were obtained using Monte Carlo simulations. Minimum-bias Pb–Pb collisions at $\sqrt{s_{\text{NN}}} = 2.76$ TeV were produced with the HIJING v1.36 event generator [38]. Prompt and feed-down (B decays) D meson signals were added using pp events from the PYTHIA v6.4.21 event generator [36] with the Perugia-0 tuning [37]. Each injected pp event was required to contain a $c\bar{c}$ or $b\bar{b}$ pair and D mesons were forced to decay in the hadronic channels of interest for the analysis. The number of pp events added to each Pb–Pb event was adjusted according to the Pb–Pb collision centrality. The simulations used the GEANT3 [39] particle transport package together with a detailed description of the geometry of the apparatus and of the detector response. The simulation was configured to reproduce the conditions of the luminous region and of all the ALICE subsystems, in terms of active electronic channels, calibration level, and their time evolution within the Pb–Pb data taking period.

The efficiencies were evaluated in centrality classes corresponding to those used in the analysis of the data in terms of charged-particle multiplicity, hence of detector occupancy. Figure 3 shows the $D^0 \rightarrow K^- \pi^+$, $D^+ \rightarrow K^- \pi^+ \pi^+$, and $D^{*+} \rightarrow D^0 \pi^+$ acceptance-times-efficiency for prompt and feed-down D mesons with rapidity $|y| < y_{\text{fid}}$. The efficiencies correspond to Pb–Pb collisions in the centrality class 0–20%. The selection cuts described in Section 3 were applied. The values for the case of not applying PID are shown as well, in order to point out that this selection is about 95% efficient for the signal. For the three meson species, the acceptance-times-efficiency increases with p_t , starting from few per mil and reaching ≈ 5 –10% at high p_t . No significant difference in the acceptance-times-efficiency for particles and antiparticles was observed.

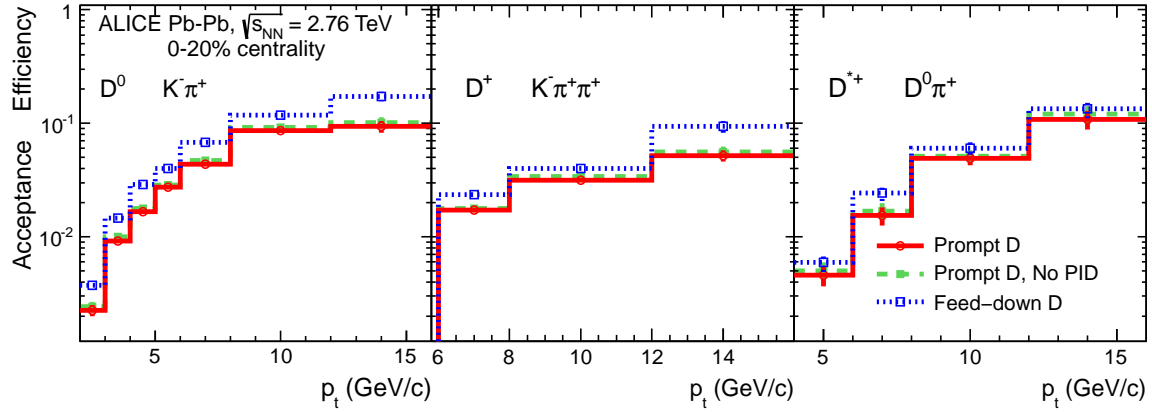


Figure 3: Acceptance-times-efficiency in Pb–Pb collisions (0–20% centrality class) for D^0 (left), D^+ (middle), and D^{*+} (right) mesons. The efficiencies for prompt (solid lines) and feed-down (dotted lines) D mesons are shown. Also displayed, for comparison, the efficiency for prompt D mesons without PID selection (dashed lines).

The acceptance-times-efficiencies for D mesons from B decays are larger than for prompt D mesons by a factor of approximately 2, because the decay vertices of the feed-down D mesons are more displaced from the primary vertex and, thus, more efficiently selected by the cuts.

In the 40–80% centrality class, as discussed in the previous Section, the selection cuts were looser, resulting in a higher efficiency. The dependence of the D meson selection efficiency on the detector occupancy was evaluated by comparing the efficiencies for central (0–20% centrality class) and peripheral (40–80% centrality class) events when applying the same selection cuts (those of the 0–20% class were used as a reference). The results showed only small variations as a function of centrality, e.g. ≈ 5 –10% for D^0 , as expected from the small variation of the single track reconstruction efficiency with centrality [18]. Indeed, also the efficiency of the topological selection is expected to be practically independent of centrality in the considered range 0–80% where the resolution on the primary vertex position is not significantly affected by the multiplicity of tracks used in its determination.

The prompt D meson production yields dN/dp_t in Pb–Pb collisions were obtained by subtracting the contribution of D mesons from B decays with the same procedure used for the measurement of the production cross sections in pp collisions [27]. In detail, the feed-down contribution was estimated using the beauty production cross section from the FONLL calculation [40], the $B \rightarrow D$ decay kinematics from the EvtGen package [41], and the Monte Carlo efficiencies for feed-down D mesons. For Pb–Pb collisions, the FONLL feed-down cross section in pp at $\sqrt{s} = 2.76$ TeV was scaled by the average nuclear overlap function $\langle T_{AA} \rangle$ in each centrality class. Thus, omitting for brevity the symbol of the p_t -dependence (p_t), the fraction of prompt D mesons reads:

$$\begin{aligned}
 f_{\text{prompt}} &= 1 - (N^{\text{D feed-down raw}} / N^{\text{D raw}}) = \\
 &= 1 - \langle T_{AA} \rangle \cdot \left(\frac{d^2\sigma}{dy dp_t} \right)_{\text{feed-down}}^{\text{FONLL}} \cdot R_{AA}^{\text{feed-down}} \cdot \frac{(\text{Acc} \times \varepsilon)_{\text{feed-down}} \cdot \Delta y \Delta p_t \cdot \text{BR} \cdot N_{\text{evt}}}{N^{\text{D raw}}/2}, \quad (3)
 \end{aligned}$$

where $(\text{Acc} \times \varepsilon)_{\text{feed-down}}$ is the acceptance-times-efficiency for feed-down D mesons. The nuclear modification factor of the feed-down D mesons, $R_{AA}^{\text{feed-down}}$, is related to the nuclear modification of beauty production in Pb–Pb collisions, which is currently unknown. We therefore assumed for the correction that the nuclear modification factors for feed-down and prompt D mesons are equal ($R_{AA}^{\text{feed-down}} = R_{AA}^{\text{prompt}}$) and varied this hypothesis in the range $1/3 < R_{AA}^{\text{feed-down}}/R_{AA}^{\text{prompt}} < 3$ to determine the systematic uncertainty. This hypothesis is justified by the range of the model predictions for the charm and beauty R_{AA} [10, 16] and, as discussed in Section 6, by the CMS Collaboration results on R_{AA} for non-prompt J/ψ [25]. The

value of f_{prompt} depends on the D meson species, the transverse momentum interval, the applied cuts, the parameters used in the FONLL B prediction, and the hypothesis on $R_{\text{AA}}^{\text{feed-down}}$. The resulting values, for the case $R_{\text{AA}}^{\text{feed-down}} = R_{\text{AA}}^{\text{prompt}}$, range from ≈ 0.95 in the lowest transverse momentum interval ($2 < p_t < 3$ GeV/ c) to ≈ 0.85 at high p_t .

5 Reference pp cross section at $\sqrt{s} = 2.76$ TeV

The reference pp cross sections used for the determination of the nuclear modification factors were obtained by applying a \sqrt{s} -scaling [42] to the cross sections measured at $\sqrt{s} = 7$ TeV [27]. The scaling factor for each D meson species was defined as the ratio of the cross sections from the FONLL pQCD calculations [40] at 2.76 and 7 TeV. The same values of the pQCD factorization scale μ_F and renormalization scale μ_R , and of the charm quark mass m_c were used in the calculation for the different energies. Namely, $\mu_F = \mu_R = m_t$ with $m_t = \sqrt{p_t^2 + m_c^2}$ and $m_c = 1.5$ GeV/ c^2 . The theoretical uncertainty on the scaling factor was evaluated by considering the envelope of the scaling factors resulting by varying independently the scales in the ranges $0.5 < \mu_R/m_t < 2$, $0.5 < \mu_F/m_t < 2$, with $0.5 < \mu_R/\mu_F < 2$, and the quark mass in the range $1.3 < m_c < 1.7$ GeV/ c^2 , following the prescription in [43]. This uncertainty ranges from $^{+30}_{-10}\%$ at $p_t = 2$ GeV/ c to about $\pm 5\%$ for $p_t > 10$ GeV/ c [42]. The procedure was validated by scaling the ALICE pp data to the Tevatron energy, $\sqrt{s} = 1.96$ TeV, and comparing to CDF measurements [42, 44]. In addition, it was verified that the scaling factor and its uncertainty are the same if the GM-VFNS calculation [45] is used instead of FONLL [42].

The D^0 , D^+ , and D^{*+} cross sections were measured, though with limited precision and p_t coverage, in pp collisions at $\sqrt{s} = 2.76$ TeV using a sample of about 6×10^7 minimum-bias events collected during a short run at the same energy as Pb–Pb collisions. These measurements were found to be in agreement with the scaled 7 TeV measurements, within statistical uncertainties of about 20–40% depending on p_t and on the meson species [28].

6 Systematic uncertainties

Systematic uncertainties on the Pb–Pb yields

The systematic uncertainties on the prompt D meson yields in Pb–Pb collisions are summarized in Table 3 for the lowest and highest p_t intervals in the two centrality classes 0–20% and 40–80%.

The systematic uncertainty on the yield extraction from the invariant mass spectra was determined by repeating the fit, in each p_t interval, in a different mass range and also with a different function to describe the background. Namely, a parabola, instead of an exponential, was considered for D^0 and D^+ , and a power law multiplied by an exponential or a polynomial for D^{*+} . A method based on counting the signal in the invariant mass distribution, after subtraction of the background estimated from a fit to the side bands, was also used. The uncertainty was defined as the maximum difference of these results and it was found to vary in the range 5–20%, depending on the p_t interval and on the collision centrality.

The systematic uncertainty on the tracking efficiency was estimated by comparing the efficiency (i) of track finding in the TPC and (ii) of track prolongation from the TPC to the ITS between data and simulation, and (iii) by varying the track quality selections. The efficiency of track prolongation from the TPC to the ITS and of association of hits in the silicon pixel layers was found to be described in simulation at the level of 5% in the p_t range relevant for this analysis (0.5–15 GeV/ c). The centrality dependence of these efficiencies, which is limited to $\pm 3\%$ in this p_t range, was found to be reproduced within 1.5%. The effect of wrong association of ITS hits to tracks was studied in the simulation. It was found that the fraction of D mesons with at least one decay track with wrong hit associations increases with centrality, due to the higher detector occupancy, and vanishes at large p_t , where the track extrapolation between layers is more precise. In the centrality class 0–20%, it ranges from 7% to 1% in the transverse momentum

Table 3: Summary of relative systematic uncertainties on the prompt D meson production yields in Pb–Pb collisions for the lowest and highest p_t bins measured for the three mesons.

Particle		D ⁰		D ⁺		D ^{*+}	
0–20% centrality	p_t interval (GeV/c)	2–3	12–16	6–8	12–16	4–6	12–16
	0–20% centrality	Yield extraction	8%	10%	20%	10%	20%
Tracking efficiency		10%	10%	15%	15%	15%	15%
Cut efficiency		13%	10%	15%	15%	10%	10%
PID efficiency		$+^{15}\%$ $-^5\%$	5%	5%	5%	$+^{15}\%$ $-^5\%$	5%
MC p_t shape		4%	3%	1%	5%	3%	3%
FONLL feed-down corr.		$+^2\%$ $-^{14}\%$	$+^6\%$ $-^8\%$	$+^3\%$ $-^7\%$	$+^7\%$ $-^9\%$	$+^2\%$ $-^5\%$	$+^2\%$ $-^7\%$
$R_{\text{AA}}^{\text{feed-down}}/R_{\text{AA}}^{\text{prompt}}$ (Eq. (3))		$+^4\%$ $-^{10}\%$	$+^{14}\%$ $-^{27}\%$	$+^7\%$ $-^{16}\%$	$+^{15}\%$ $-^{28}\%$	$+^4\%$ $-^9\%$	$+^5\%$ $-^{12}\%$
BR		1.3%		2.1%		1.5%	
Centrality limits		< 0.1%					
40–80% centrality	p_t interval (GeV/c)	2–3	12–16	3–4	8–12	2–4	12–16
	Yield extraction	5%	5%	15%	15%	15%	8%
	Tracking efficiency	10%	10%	15%	15%	15%	15%
	Cut efficiency	13%	10%	10%	10%	10%	10%
	PID efficiency	$+^{10}\%$ $-^5\%$	5%	5%	5%	$+^{10}\%$ $-^5\%$	5%
	MC p_t shape	1%	3%	1%	3%	5%	4%
	FONLL feed-down corr.	$+^3\%$ $-^{16}\%$	$+^4\%$ $-^5\%$	$+^3\%$ $-^{11}\%$	$+^4\%$ $-^9\%$	$+^1\%$ $-^8\%$	$+^1\%$ $-^4\%$
	$R_{\text{AA}}^{\text{feed-down}}/R_{\text{AA}}^{\text{prompt}}$ (Eq. (3))	$+^5\%$ $-^{12}\%$	$+^{11}\%$ $-^{22}\%$	$+^6\%$ $-^{14}\%$	$+^9\%$ $-^{20}\%$	$+^2\%$ $-^6\%$	$+^3\%$ $-^8\%$
	BR	1.3%		2.1%		1.5%	
Centrality limits	3%						

interval $2 < p_t < 16$ GeV/c. However, it was verified that the signal selection efficiencies are compatible, within statistical uncertainties, between D mesons with and without wrong hit associations. Indeed, the mis-associated hit is typically very close in space to the correct hit. Overall, the systematic uncertainty from track reconstruction amounts to 5% for single tracks, which results in a 10% uncertainty for D⁰ mesons (two-track final state) and 15% uncertainty for D⁺ and D^{*+} mesons (three-track final state).

The uncertainty on the correction for the selection cut efficiency was evaluated by repeating the analysis with different sets of cuts and was defined as the variation of the resulting corrected yields about the value corresponding to the central set. This resulted in 13% for D⁰ for $p_t < 3$ GeV/c, 15% for D⁺ in all p_t intervals in the 0–20% centrality class, and 10% for the other cases (see Table 3). Part of this uncertainty comes from residual detector misalignment effects not fully described in the simulation. In order to estimate this contribution, the secondary vertices in the simulation were also reconstructed after scaling, for each track, the impact parameter residuals with respect to their true value. In particular, a scaling factor of 1.1–1.2 was applied in order to reproduce the impact parameter resolution observed in the data (see Fig. 1). The relative variation of the efficiency is 8% for $p_t = 2–3$ GeV/c and negligible for $p_t > 5$ GeV/c. This effect was not included explicitly in the systematic uncertainty, since it is already accounted for in the cut variation study. A further check was performed by comparing the distributions of the cut variables used for the candidate selection in the data and in the simulation. These comparisons can only be carried out by releasing the selection, hence essentially for background candidates. However, they provide an indication of the level of accuracy of the simulation. A good agreement was observed,

with no dependence on collision centrality.

The uncertainty arising from the PID selection was estimated by comparing the corrected signals extracted with and without this selection. In the 20% most central collisions, it was found to be $+15\%$ for $p_t < 6$ GeV/ c and $\pm 5\%$ for $p_t > 6$ GeV/ c . In the 40–80% centrality range, it was estimated to be $\pm 5\%$ for $p_t > 3$ GeV/ c and $+10\%$ in $2 < p_t < 3$ GeV/ c .

The uncertainty on the efficiencies arising from the difference between the real and simulated shape of the D meson transverse momentum distribution, which includes also the effect of the p_t dependence of the nuclear modification factor, depends on the width of the p_t intervals and on the slope of the efficiencies with p_t . It was estimated by varying the simulated shape between the PYTHIA and FONLL dN/dp_t , with and without the nuclear modification observed in the data. The resulting uncertainty is below 5% in all the p_t intervals considered for the three meson species. As an example, for D^0 it is 4% in the lowest and highest p_t intervals (2–3 GeV/ c and 12–16 GeV/ c) and 1% in 3–12 GeV/ c .

The p_t -differential yields for D^0 and \bar{D}^0 mesons, extracted separately, were found to be in agreement within the statistical uncertainties of about 20–25%. Due to the limited statistics, this check could not be carried out for D^+ and D^{*+} mesons.

The systematic uncertainty from the subtraction of feed-down D mesons from B decays was estimated as for the pp case [27]. The contribution of the FONLL perturbative uncertainties was included by varying the heavy quark masses and the factorization and renormalization scales in the ranges proposed in [43]. Furthermore, a different procedure was used to evaluate the prompt fraction. In this approach, the ratio of the FONLL feed-down and prompt production cross sections is the input for evaluating the correction factor. Then, the prompt fraction depends explicitly on the ratio of nuclear modification factors of feed-down and prompt D mesons:

$$f'_{\text{prompt}} = \left(1 + \frac{(\text{Acc} \times \varepsilon)_{\text{feed-down}}}{(\text{Acc} \times \varepsilon)_{\text{prompt}}} \cdot \frac{\left(\frac{d^2\sigma}{dy dp_t} \right)_{\text{feed-down}}^{\text{FONLL}}}{\left(\frac{d^2\sigma}{dy dp_t} \right)_{\text{prompt}}^{\text{FONLL}}} \cdot \frac{R_{AA}^{\text{feed-down}}}{R_{AA}^{\text{prompt}}} \right)^{-1}. \quad (4)$$

The systematic uncertainty due to the B feed-down subtraction was evaluated as the envelope of the results obtained with the two methods, Eqs. (3) and (4), when varying the FONLL parameters. The

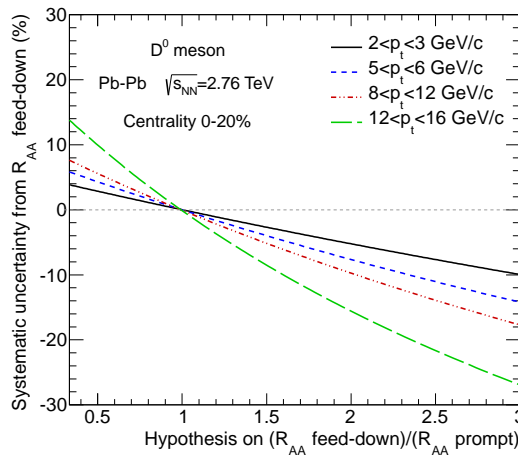


Figure 4: Relative variation of the prompt D^0 meson yield as a function of the hypothesis on $R_{AA}^{\text{feed-down}}/R_{AA}^{\text{prompt}}$ for the B feed-down subtraction approach based on Eq. (3).

Table 4: Summary of relative systematic uncertainties on R_{AA} . For the data systematic uncertainties and the B feed-down subtraction some of the contributions are singled-out in the indented rows.

Particle		D ⁰		D ⁺		D ^{*+}	
0–20% centrality	p_t interval (GeV/c)	2–3	12–16	6–8	12–16	4–6	12–16
	Data syst. pp and Pb–Pb	+33% –41%	+28% –28%	+35% –35%	+35% –35%	+42% –41%	+34% –35%
	Data syst. in Pb–Pb	+26% –22%	+22% –22%	+30% –30%	+27% –27%	+39% –36%	+29% –29%
	Data syst. in pp	17%	17%	15%	21%	15%	18%
	\sqrt{s} -scaling of the pp ref.	+10% –31%	+5% –6%	+6% –10%	+4% –6%	+7% –14%	+5% –6%
	Feed-down subtraction	+15% –14%	+16% –29%	+12% –18%	+17% –28%	+5% –12%	+8% –16%
	FONLL feed-down corr.	+12% –2%	+1% –2%	+3% –2%	+2% –1%	+1% –1%	+2% –1%
	$R_{AA}^{\text{feed-down}}/R_{AA}^{\text{prompt}}$ (Eq. (3))	+4% –10%	+14% –27%	+7% –16%	+15% –28%	+4% –9%	+5% –12%
Normalization	5.3%						
40–80% centrality	p_t interval (GeV/c)	2–3	12–16	3–4	8–12	2–4	12–16
	Data syst. pp and Pb–Pb	+28% –40%	+24% –25%	+40% –43%	+30% –31%	+33% –39%	+29% –30%
	Data syst. in Pb–Pb	+21% –19%	+17% –17%	+25% –25%	+24% –24%	+28% –27%	+22% –22%
	Data syst. in pp	17%	17%	30%	17%	15%	18%
	\sqrt{s} -scaling of the pp ref.	+10% –31%	+5% –6%	+8% –19%	+5% –8%	+10% –24%	+5% –6%
	Feed-down subtraction	+13% –17%	+12% –23%	+10% –18%	+15% –25%	+3% –13%	+3% –14%
	FONLL feed-down corr.	+10% –2%	+1% –1%	+4% –1%	+2% –1%	+1% –5%	+1% –3%
	$R_{AA}^{\text{feed-down}}/R_{AA}^{\text{prompt}}$ (Eq. (3))	+5% –12%	+11% –22%	+6% –14%	+9% –20%	+2% –6%	+3% –8%
Normalization	7.5%						

resulting uncertainty ranges between $^{+2}_{-14}\%$ at low p_t and $^{+6}_{-8}\%$ at high p_t (for D⁰ in the 0–20% centrality class).

The contribution from the different nuclear modification factors of prompt and feed-down D mesons was evaluated by varying the hypothesis on $R_{AA}^{\text{feed-down}}/R_{AA}^{\text{prompt}}$ in the range $1/3 < R_{AA}^{\text{feed-down}}/R_{AA}^{\text{prompt}} < 3$ for both feed-down subtraction methods. The resulting uncertainty is at most 30%, as shown in Fig. 4, where the relative prompt D⁰ yield variation is displayed as a function of $R_{AA}^{\text{feed-down}}/R_{AA}^{\text{prompt}}$ for four p_t intervals using the B feed-down subtraction approach based on Eq. (3). Considering the resulting values of R_{AA}^{prompt} shown in the next section, the variation of the hypothesis on $R_{AA}^{\text{feed-down}}/R_{AA}^{\text{prompt}}$ corresponds, for the 20% most central collisions, to values of the nuclear modification factor of D mesons from B feed-down in a range of about 0.17–1.5 at low p_t and 0.09–0.8 at high p_t . The R_{AA} of non-prompt J/ψ, measured by CMS [25], falls in this range as well as the available model predictions for B meson energy loss [10, 16].

The contribution due to the 1.1% relative uncertainty on the fraction of hadronic cross section used in the Glauber fit to determine the centrality classes was obtained by estimating the variation of the D meson dN/dp_t when the limits of the centrality classes are shifted by $\pm 1.1\%$ (e.g., for the 40–80% class, 40.4–80.9% and 39.6–79.1%). The resulting uncertainty is common to all meson species and all p_t bins for a given centrality class. It increases from central to peripheral events. In particular, it is less than 0.1% in the 0–20% centrality class and 3% in 40–80%.

Finally, the systematic uncertainty on the branching ratios [35] was considered.

Systematic uncertainties on R_{AA}

The systematic uncertainties on the R_{AA} measurement derive from the uncertainties on: the reference

cross section for pp collisions, the Pb–Pb yields, and the average nuclear overlap function for the various centrality classes, as given in Table 1. For the pp reference, the uncertainties on the measurement at $\sqrt{s} = 7$ TeV were quantified in [27] and the scaling to $\sqrt{s} = 2.76$ TeV, described in Section 5, introduces additional uncertainties of about 10–30%. The uncertainties on the Pb–Pb prompt D meson yields were described previously in this section. For the nuclear modification factor, the pp and Pb–Pb uncertainties were added in quadrature, except for the feed-down contribution deriving from FONLL uncertainties, that partly cancels in the ratio. This contribution was evaluated by comparing the R_{AA} values obtained with the two methods for feed-down correction described above and with the different heavy quark masses, factorization and renormalization scales used in FONLL. In this study, the same method and the same set of FONLL parameters were used for pp and Pb–Pb, so as to take into account the correlations of these sources in the numerator and denominator of R_{AA} .

The resulting systematic uncertainties are summarized in Table 4. In the table, the normalization uncertainty is the quadratic sum of the 3.5% pp normalization uncertainty [27], the contribution due to the 1.1% uncertainty on the fraction of hadronic cross section used in the Glauber fit discussed above, and the uncertainty on $\langle T_{AA} \rangle$, which is 3.9% for the centrality class 0–20% and 5.9% for the 40–80% class.

7 Results

7.1 D meson p_t spectra and R_{AA}

The transverse momentum distributions dN/dp_t of prompt D^0 , D^+ , and D^{*+} mesons are presented in Fig. 5, for the centrality classes 0–20% and 40–80%. The spectra from Pb–Pb collisions, defined as the feed-down corrected production yields per event (see Eq. (2)), are compared to the reference spectra from pp collisions, which are constructed as $\langle T_{AA} \rangle d\sigma/dp_t$, using the \sqrt{s} -scaled pp measurements at 7 TeV [27] and the average nuclear overlap function values from Table 1. A clear suppression is observed in Pb–Pb collisions, which is stronger in central than in peripheral collisions.

The ratio of the Pb–Pb to the reference spectra provides the nuclear modification factors $R_{AA}(p_t)$ of prompt D^0 , D^+ , and D^{*+} mesons, which are shown for central (0–20%) and semi-peripheral (40–80%) collisions in Fig. 6. The vertical bars represent the statistical uncertainties, typically about 20–25% for D^0 and about 30–40% for D^+ and D^{*+} mesons in central collisions. The total p_t -dependent systematic uncertainties, shown as empty boxes, include all the contributions described in the previous section, except for the normalization uncertainty, which is displayed as a filled box at $R_{AA} = 1$. The results for the three D meson species are in agreement within statistical uncertainties and they show a suppression reaching a factor 3–4 ($R_{AA} \approx 0.25$ –0.3) in central collisions for $p_t > 5$ GeV/ c . For decreasing p_t , the D^0 R_{AA} in central collisions shows a tendency to less suppression.

The centrality dependence of the nuclear modification factor was studied in the two wider transverse momentum intervals $2 < p_t < 5$ GeV/ c , for D^0 , and $6 < p_t < 12$ GeV/ c , for the three D meson species. This study was performed in five centrality classes from 0–10% to 60–80% (see Table 1). The invariant mass analysis and all the corrections were carried out as described in Sections 3 and 4. The systematic uncertainties are essentially the same as for the p_t -dependence analysis, except for the contribution from the D meson p_t -shape in the simulation, which is larger in the wide intervals. It amounts to 8% for D^0 , 10% for D^+ , and 5–15% (depending on centrality) for D^{*+} mesons in $6 < p_t < 12$ GeV/ c . In the transverse momentum interval 2–5 GeV/ c , this uncertainty is larger (8–17%, depending on centrality) due to the larger contribution from the p_t dependence of the nuclear modification factor. The resulting R_{AA} is shown in Fig. 7 as a function of the average number of participants, $\langle N_{part} \rangle$. The contribution to the systematic uncertainty that is fully correlated between centrality classes (normalization and pp reference cross-section) and the remaining, uncorrelated, systematic uncertainties are displayed separately, by the filled and empty boxes, respectively. The contribution from feed-down correction was considered among the uncorrelated sources because it is dominated by the variation of the ratio $R_{AA}^{\text{feed-down}}/R_{AA}^{\text{prompt}}$, which

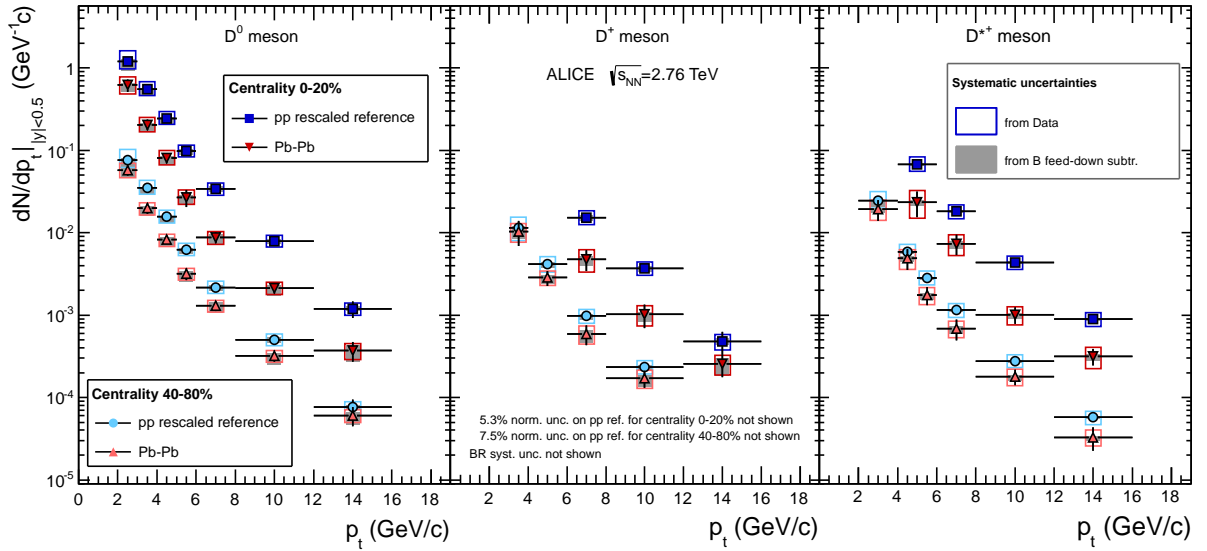


Figure 5: (colour online) Transverse momentum distributions dN/dp_t of prompt D^0 (left) and D^+ (centre), and D^{*+} (right) mesons in the 0–20% and 40–80% centrality classes in Pb–Pb collisions at $\sqrt{s_{NN}} = 2.76$ TeV. The reference pp distributions $\langle T_{AA} \rangle d\sigma/dp_t$ are shown as well. Statistical uncertainties (bars) and systematic uncertainties from data analysis (empty boxes) and from feed-down subtraction (full boxes) are shown. For Pb–Pb, the latter includes the uncertainties from the FONLL feed-down correction and from the variation of the hypothesis on $R_{AA}^{\text{prompt}}/R_{AA}^{\text{feed-down}}$. Horizontal error bars reflect bin widths, symbols were placed at the centre of the bin.

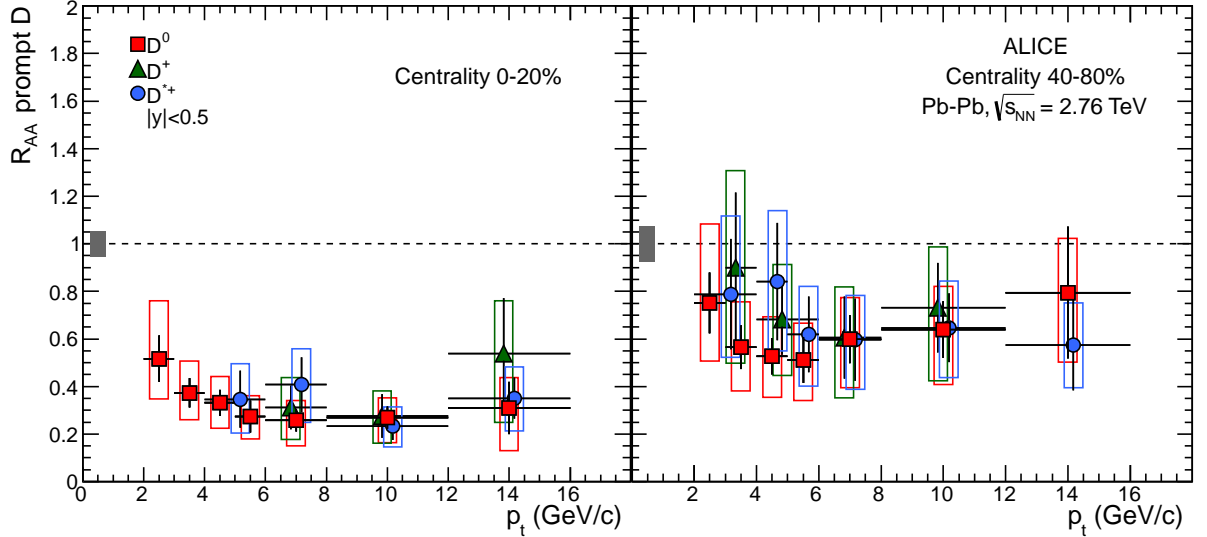


Figure 6: (colour online) R_{AA} for prompt D^0 , D^+ , and D^{*+} in the 0–20% (left) and 40–80% (right) centrality classes. Statistical (bars), systematic (empty boxes), and normalization (full box) uncertainties are shown. Horizontal error bars reflect bin widths, symbols were placed at the centre of the bin.

may depend on centrality. For the p_t interval 6–12 GeV/c, the suppression increases with increasing centrality. It is interesting to note that the suppression of prompt D mesons at central rapidity and high transverse momentum, shown in the right-hand panel of Fig. 7 is very similar, both in size and centrality dependence, to that of prompt J/ψ mesons in a similar p_t range and $|y| < 2.4$, recently measured by the CMS Collaboration [25].

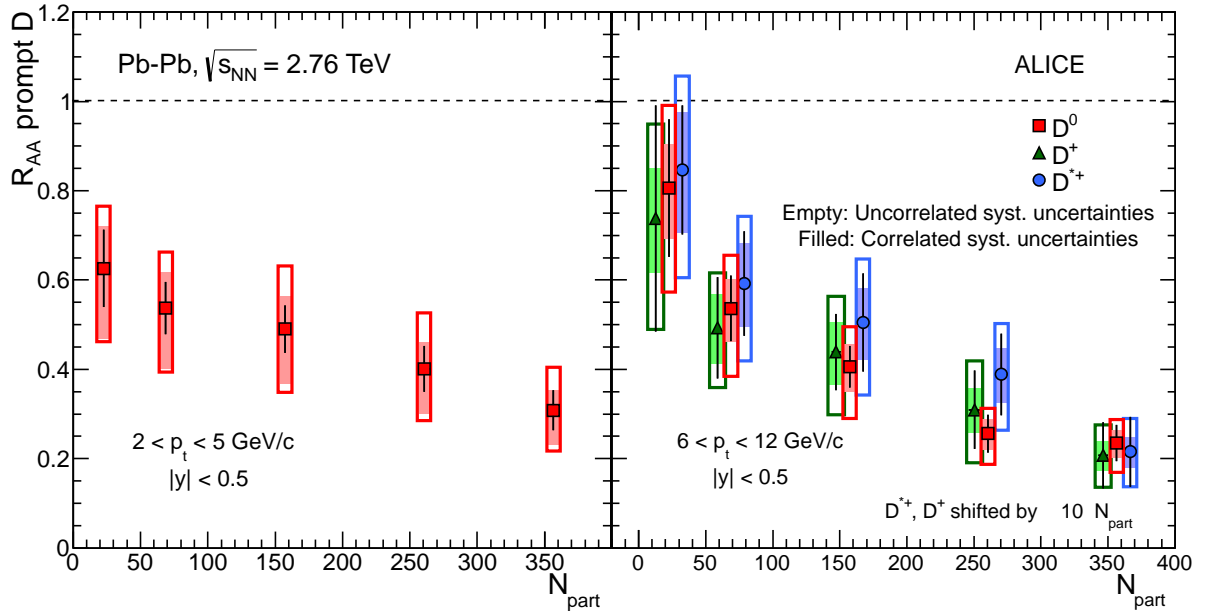


Figure 7: Centrality dependence of R_{AA} for prompt D mesons. Left: D^0 mesons with $2 < p_t < 5$ GeV/c. Right: D^0 , D^+ , and D^{*+} mesons with $6 < p_t < 12$ GeV/c. D^+ and D^{*+} points are displaced horizontally for better visibility.

7.2 Comparisons to light-flavour hadrons and with models

In this section, the average nuclear modification factor of the three D meson species is compared to that of charged particles [19], mainly light-flavour hadrons, and to model calculations. The contributions of D^0 , D^+ , and D^{*+} to the average were weighted by their statistical uncertainties. Therefore, the resulting R_{AA} is close to that of the D^0 meson, which has the smallest uncertainties. The systematic errors were calculated by propagating the uncertainties through the weighted average, where the contributions from the tracking efficiency, from the B feed-down correction, and from the FONLL scaling of 7 TeV data to 2.76 TeV were taken as fully correlated among the three D meson species. The possible statistical correlation between the D^0 and D^{*+} R_{AA} , induced by the $D^{*+} \rightarrow D^0 \pi^+$ decay, is negligible, because the statistical uncertainties, used as weights, are mainly determined by the background uncertainties, which are uncorrelated. The resulting values are shown in Table 5 for the two centrality classes where R_{AA} was measured as a function of p_t , and in Table 6 for the R_{AA} as a function of centrality in the transverse momentum range $6 < p_t < 12$ GeV/c.

In addition to final state effects, where parton energy loss would be predominant, also initial-state effects are expected to influence the measured R_{AA} . In particular, the nuclear modification of the parton distribution functions of the nucleons in the two colliding nuclei modifies the initial hard scattering probability and, thus, the production yields of hard partons, including heavy quarks. In the kinematic range relevant for charm production at LHC energies, the main expected effect is nuclear shadowing, which reduces the parton distribution functions for partons with nucleon momentum fraction x below 10^{-2} . The effect of shadowing on the D meson R_{AA} was estimated using the next-to-leading order (NLO) perturbative QCD calculation by Mangano, Nason, and Ridolfi (MNR) [46] with CTEQ6M parton distribution functions [47] and the EPS09NLO parametrization [48] of their nuclear modification. The uncertainty band determined by the EPS09 uncertainties is shown in the left-hand panel of Fig. 8, together with the average D meson R_{AA} . The shadowing-induced effect on the R_{AA} is limited to $\pm 15\%$ for $p_t > 6$ GeV/c, suggesting that the strong suppression observed in the data is a final-state effect.

The expected colour charge and parton mass dependences of parton energy loss should be addressed

Table 5: Average R_{AA} as a function of p_t for prompt D mesons in the 0–20% and 40–80% centrality classes. The systematic error does not include the normalization uncertainty, which is $\pm 5.3\%$ ($\pm 7.5\%$) for the 0–20% (40–80%) centrality class.

p_t interval (GeV/ c)	$R_{\text{AA}} \pm \text{stat} \pm \text{syst}$	
	0–20% centrality	40–80% centrality
2–3	$0.51 \pm 0.10^{+0.18}_{-0.22}$	$0.75 \pm 0.13^{+0.23}_{-0.32}$
3–4	$0.37 \pm 0.06^{+0.11}_{-0.13}$	$0.59 \pm 0.09^{+0.15}_{-0.21}$
4–5	$0.33 \pm 0.05^{+0.10}_{-0.11}$	$0.55 \pm 0.07^{+0.14}_{-0.18}$
5–6	$0.27 \pm 0.07^{+0.08}_{-0.09}$	$0.54 \pm 0.08^{+0.13}_{-0.17}$
6–8	$0.28 \pm 0.04^{+0.07}_{-0.08}$	$0.60 \pm 0.08^{+0.14}_{-0.18}$
8–12	$0.26 \pm 0.03^{+0.06}_{-0.07}$	$0.66 \pm 0.08^{+0.16}_{-0.20}$
12–16	$0.35 \pm 0.06^{+0.10}_{-0.12}$	$0.64 \pm 0.16^{+0.16}_{-0.18}$

Table 6: Average R_{AA} as a function of centrality for prompt D mesons in the transverse momentum interval $6 < p_t < 12$ GeV/ c .

Centrality	$R_{\text{AA}} \pm \text{stat} \pm \text{syst(uncorr)} \pm \text{syst(corr)}$
0–10%	$0.23 \pm 0.03^{+0.05}_{-0.06}^{+0.03}_{-0.03}$
10–20%	$0.28 \pm 0.04^{+0.06}_{-0.07}^{+0.03}_{-0.04}$
20–40%	$0.42 \pm 0.04^{+0.08}_{-0.11}^{+0.05}_{-0.06}$
40–60%	$0.54 \pm 0.05^{+0.10}_{-0.13}^{+0.07}_{-0.08}$
60–80%	$0.81 \pm 0.10^{+0.16}_{-0.21}^{+0.11}_{-0.12}$

by comparing the nuclear modification factor of D and π mesons. Since final results on the pion R_{AA} at the LHC are not yet available, we compare here to charged particles. Preliminary results [49] have shown that the charged-pion R_{AA} coincides with that of charged particles above $p_t \approx 5$ GeV/ c and it is lower by 30% at 3 GeV/ c . The comparison between D meson and charged particle R_{AA} , reported in the right-hand panel of Fig. 8, shows that the average D meson nuclear modification factor is close to that of charged particles [19]. However, considering that the systematic uncertainties of D mesons are not fully correlated with p_t , there is an indication for $R_{\text{AA}}^{\text{D}} > R_{\text{AA}}^{\text{charged}}$. In the same figure, the nuclear modification factor measured by the CMS Collaboration for non-prompt J/ψ mesons (from B decays) with $p_t > 6.5$ GeV/ c [25] is also shown. Their suppression is clearly weaker than that of charged particles, while the comparison with D mesons is not conclusive and would require more differential and precise measurements of the transverse momentum dependence.

Several theoretical models based on parton energy loss compute the charm nuclear modification factor: (I) [13, 50], (II) [51], (III) [52], (IV) [53], (V) [54], (VI) [55], (VII) [56], (VIII) [16]. Figure 9 displays the comparison of these models to the average D meson R_{AA} , for central Pb–Pb collisions (0–20%), along with the comparison to the charged-particle R_{AA} [19], for those models that also compute this observable: (I) [13], (II) [51], (III) [52], (VII) [56]. Among the models that compute both observables, radiative energy loss supplemented with in-medium D meson dissociation (I) [13] and radiative plus collisional energy loss in the WHDG (II) [51] and CUJET1.0 (VII) [56] implementations describe reasonably well at the same time the charm and light-flavour suppression. While in the former calculation the medium density is tuned to describe the inclusive jet suppression at the LHC [50], for the latter two it is extrapolated to LHC conditions starting from the value that describes the pion suppression at RHIC energy ($\sqrt{s_{\text{NN}}} = 200$ GeV). This could explain why these two models are somewhat low with respect to the charged-particle R_{AA} data. A model based on AdS/CFT drag coefficients (III) [52] underestimates

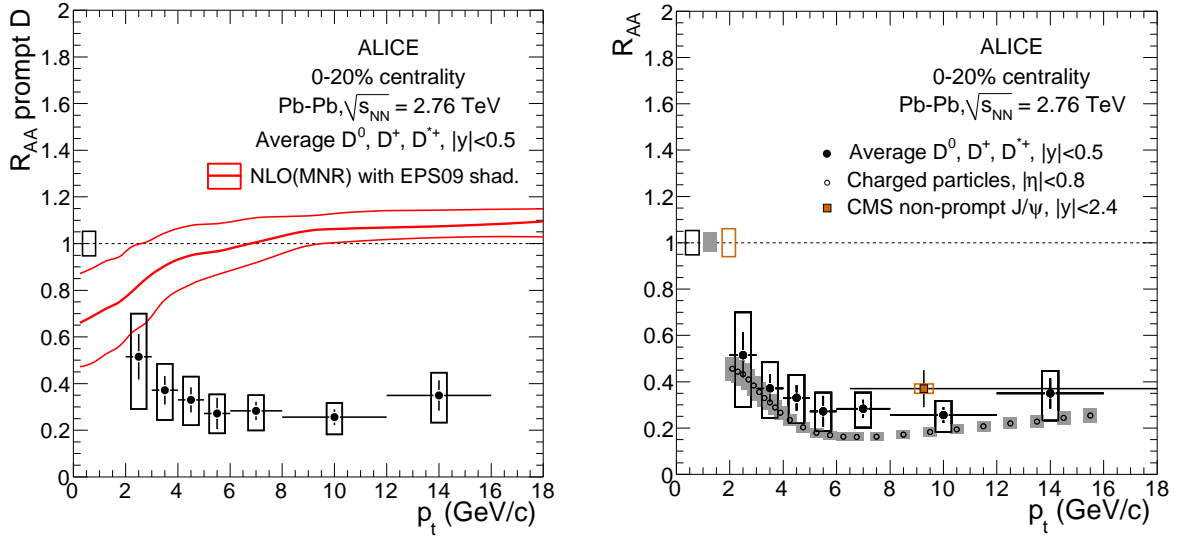


Figure 8: Average R_{AA} of D mesons in the 0–20% centrality class compared to: left, the expectation from NLO pQCD [46] with nuclear shadowing [48]; right, the nuclear modification factors of charged particles [19] and non-prompt J/ψ from B decays [25] in the same centrality class. The charged particle R_{AA} is shown only for $2 < p_t < 16$ GeV/c. The three normalization uncertainties shown in the right-hand panel are almost fully correlated.

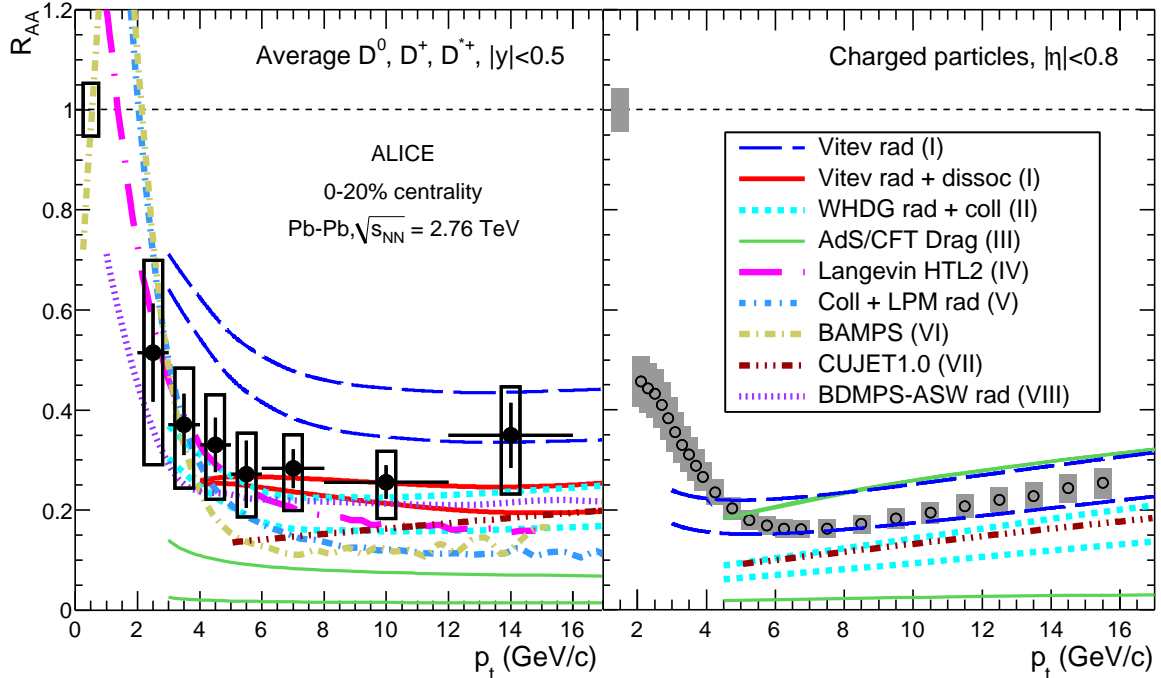


Figure 9: (colour online) Average R_{AA} of D mesons (left) and R_{AA} of charged particles (right) [19] in the 0–20% centrality class compared to model calculations: (I) [13, 50], (II) [51], (III) [52], (IV) [53], (V) [54], (VI) [55], (VII) [56], (VIII) [16]. The two normalization uncertainties are almost fully correlated.

significantly the charm R_{AA} and has very limited predictive power for the light-flavour R_{AA} .

8 Summary

The first ALICE results on the nuclear modification factor R_{AA} for charm hadrons in Pb–Pb collisions at a centre-of-mass energy $\sqrt{s_{NN}} = 2.76$ TeV indicate strong in-medium energy loss for charm quarks. The D^0 , D^+ , and D^{*+} R_{AA} , measured for the first time as a function of transverse momentum and centrality, is in the range 0.25–0.35 for $5 < p_t < 16$ GeV/ c for the 20% most central collisions. For p_t below 5 GeV/ c , and towards peripheral collisions, there is a tendency for an increase of R_{AA} for D^0 mesons.

The suppression is almost as large as that observed for charged particles, which are mainly light-flavour hadrons, with a possible indication, not fully significant with the present level of experimental uncertainties, of $R_{AA}^D > R_{AA}^{\text{charged}}$. The expected effect of PDF nuclear shadowing is small ($< 15\%$) above $p_t = 6$ GeV/ c , indicating that the large measured suppression cannot be explained by initial-state effects. Some of the pQCD models based on various implementations of parton energy loss succeed reasonably well at describing simultaneously the suppression of light flavour and charm hadrons.

The precision of the measurements will be improved in the future, using the large sample of Pb–Pb collisions recorded in 2011. In addition, p–Pb collision data expected in 2013 will provide insight on possible initial-state effects in the low-momentum region.

References

- [1] F. Karsch, J. Phys. Conf. Ser. **46** (2006) 122.
- [2] S. Borsanyi *et al.* [Wuppertal-Budapest Collaboration], JHEP **1009** (2010) 073;
S. Borsanyi, G. Endrodi, Z. Fodor, A. Jakovac, S. D. Katz, S. Krieg, C. Ratti and K. K. Szabo, JHEP **1011** (2010) 077.
- [3] A. Bazavov *et al.*, Phys. Rev. D **85** (2012) 054503.
- [4] M. Gyulassy and M. Plumer, Phys. Lett. **B243** (1990) 432.
- [5] R. Baier, Y. L. Dokshitzer, A. H. Mueller, S. Peigne and D. Schiff, Nucl. Phys. **B484** (1997) 265.
- [6] M. H. Thoma and M. Gyulassy, Nucl. Phys. **B351** (1991) 491.
E. Braaten and M. H. Thoma, Phys. Rev. **D44** (1991) 1298; Phys. Rev. **D44** (1991) 2625.
- [7] Y. L. Dokshitzer, D. E. Kharzeev, Phys. Lett. **B519** (2001) 199.
- [8] N. Armesto, C. A. Salgado and U. A. Wiedemann, Phys. Rev. **D69** (2004) 114003.
- [9] M. Djordjevic, M. Gyulassy, Nucl. Phys. **A733** (2004) 265.
- [10] S. Wicks, W. Horowitz, M. Djordjevic and M. Gyulassy, Nucl. Phys. **A783** (2007) 493.
- [11] B.-W. Zhang, E. Wang and X.-N. Wang, Phys. Rev. Lett. **93** (2004) 072301.
- [12] A. Adil and I. Vitev, Phys. Lett. **B649** (2007) 139.
- [13] R. Sharma, I. Vitev and B. -W. Zhang, Phys. Rev. **C80** (2009) 054902.
- [14] H. van Hees, V. Greco and R. Rapp, Phys. Rev. **C73** (2006) 034913.
- [15] R. J. Glauber in Lectures in Theoretical Physics, NY, 1959, Vol. 1, 315.
M. Miller *et al.*, Ann. Rev. Nucl. Part. Sci. **57** (2007) 205.
- [16] N. Armesto, A. Dainese, C. A. Salgado and U. A. Wiedemann, Phys. Rev. **D71** (2005) 054027.
- [17] I. Arsene *et al.* [BRAHMS Collaboration], Nucl. Phys. **A757** (2005) 1-27.
K. Adcox *et al.* [PHENIX Collaboration], Nucl. Phys. **A757** (2005) 184-283.
B. B. Back *et al.* [PHOBOS Collaboration], Nucl. Phys. **A757** (2005) 28-101.
J. Adams *et al.* [STAR Collaboration], Nucl. Phys. **A757** (2005) 102-183.

- [18] K. Aamodt *et al.* [ALICE Collaboration], Phys. Lett **B696** (2011) 30-39.
- [19] B. Abelev *et al.* [The ALICE Collaboration], arXiv:1208.2711 [hep-ex].
- [20] S. Chatrchyan *et al.* [CMS Collaboration], Eur. Phys. J. C **72** (2012) 1945.
- [21] S. S. Adler *et al.* [PHENIX Collaboration], Phys. Rev. Lett. **96** (2006) 032301.
A. Adare *et al.* [PHENIX Collaboration], Phys. Rev. C **84** (2011) 044905.
- [22] B. I. Abelev *et al.* [STAR Collaboration] Phys. Rev. Lett. **98** (2007) 192301.
- [23] N. Armesto, M. Cacciari, A. Dainese, C.A. Salgado and U.A. Wiedemann, Phys. Lett. **B637** (2006) 362.
- [24] N. Armesto, M. Cacciari, T. Hirano, J.L. Nagle, C.A. Salgado, J. Phys. **G37** (2010) 025104.
- [25] CMS Collaboration, arXiv:1201.5069 [nucl-ex] (2012).
- [26] K. Aamodt *et al.* [ALICE Collaboration], JINST **3** (2008) S08002.
- [27] B. I. Abelev *et al.* [ALICE Collaboration], JHEP **01** (2012) 128.
- [28] B. I. Abelev *et al.* [ALICE Collaboration], JHEP **07** (2012) 191.
- [29] K. Aamodt *et al.* [ALICE Collaboration], Phys. Rev. Lett. **105** (2010) 252301.
- [30] K. Aamodt *et al.* [ALICE Collaboration], Phys. Rev. Lett. **106** (2011) 032301.
- [31] J. Alme *et al.*, Nucl. Instrum. Meth. **A622** (2010) 316.
- [32] K. Aamodt *et al.* [ALICE Collaboration], JINST **5** (2010) P03003.
- [33] A. Rossi *et al.* [ALICE Collaboration], PoS(Vertex2010)017, arXiv:1101.3491 (2011).
- [34] A. Akindinov *et al.*, Nucl. Instrum. Meth. **A615** (2010) 37.
- [35] K. Nakamura *et al.*, [Particle Data Group], J. Phys. **G37** (2010) 075021.
- [36] T. Sjöstrand, S. Mrenna, P. Skands, JHEP **05** (2006) 026.
- [37] P. Z. Skands, arXiv:0905.3418 [hep-ph] (2009).
- [38] X.-N. Wang and M. Gyulassy, Phys. Rev. **D 44** (1991) 3501.
- [39] R. Brun *et al.*, CERN Program Library Long Write-up, W5013, GEANT Detector Description and Simulation Tool (1994).
- [40] M. Cacciari, M. Greco, P. Nason, JHEP **9805** (1998) 007.
M. Cacciari, S. Frixione and P. Nason, JHEP **0103** (2001) 006.
M. Cacciari, S. Frixione, N. Houdeau, M. L. Mangano, P. Nason and G. Ridolfi, CERN-PH-TH/2011-227, arXiv:1205.6344 [hep-ph].
M. Cacciari, private communication.
- [41] D. J. Lange, Nucl. Instrum. Methods **A462** (2001) 152.
- [42] R. Averbeck, N. Bastid, Z. Conesa del Valle, A. Dainese, X. Zhang, arXiv:1107.3243 (2011).
- [43] M. Cacciari, P. Nason, and R. Vogt, Phys. Rev. Lett. **95** (2005) 122001.
- [44] D. Acosta *et al.* [CDF Collaboration], Phys. Rev. Lett. **91** (2003) 241804.
- [45] B.A. Kniehl *et al.*, Phys. Rev. Lett. **96** (2006) 012001.
B. A. Kniehl, G. Kramer, I. Schienbein and H. Spiesberger, Eur. Phys. J. C **72** (2012) 2082, DESY 12-013, MZ-TH/12-07, LPSC 12019, arXiv:1202.0439 [hep-ph].
H. Spiesberger, private communication.
- [46] M. Mangano, P. Nason and G. Ridolfi, Nucl. Phys. **B373** (1992) 295.
- [47] J. Pumplin *et al.*, JHEP **0207** (2002) 012.
- [48] K. J. Eskola, H. Paukkunen and C. A. Salgado, JHEP **0904** (2009) 065.
- [49] H. Appelshauser for the ALICE Collaboration, J. Phys. **G38** (2011) 124014.
- [50] Y. He, I. Vitev and B. -W. Zhang, Phys. Lett. B **713** (2012) 224.
- [51] W. A. Horowitz and M. Gyulassy, J. Phys. **G38** (2011) 124114.
- [52] W. A. Horowitz, arXiv:1108.5876 [hep-ph] (2011).

- [53] W. M. Alberico, *et al.*, Eur. Phys. J. **C71** (2011) 1666; J. Phys. **G38** (2011) 124144.
[54] P. B. Gossiaux, R. Bierkanth and J. Aichelin, Phys. Rev. **C79** (2009) 044906.
P. B. Gossiaux, J. Aichelin, T. Gousset and V. Guiho, J. Phys. **G37** (2010) 094019.
[55] O. Fochler, J. Uphoff, Z. Xu and C. Greiner, J. Phys. **G38** (2011) 124152.
[56] A. Buzzatti and M. Gyulassy, Phys. Rev. Lett. **108** (2012) 022301.

Acknowledgements

The ALICE collaboration would like to thank all its engineers and technicians for their invaluable contributions to the construction of the experiment and the CERN accelerator teams for the outstanding performance of the LHC complex. The ALICE Collaboration would like to thank M. Cacciari and H. Spiesberger for providing the pQCD predictions used for the feed-down correction and the energy scaling, and the authors of the energy loss model calculations for making available their predictions for the nuclear modification factor.

The ALICE collaboration acknowledges the following funding agencies for their support in building and running the ALICE detector:

Calouste Gulbenkian Foundation from Lisbon and Swiss Fonds Kidagan, Armenia;

Conselho Nacional de Desenvolvimento Científico e Tecnológico (CNPq), Financiadora de Estudos e Projetos (FINEP), Fundação de Amparo à Pesquisa do Estado de São Paulo (FAPESP);

National Natural Science Foundation of China (NSFC), the Chinese Ministry of Education (CMOE) and the Ministry of Science and Technology of China (MSTC);

Ministry of Education and Youth of the Czech Republic;

Danish Natural Science Research Council, the Carlsberg Foundation and the Danish National Research Foundation;

The European Research Council under the European Community's Seventh Framework Programme;

Helsinki Institute of Physics and the Academy of Finland;

French CNRS-IN2P3, the 'Region Pays de Loire', 'Region Alsace', 'Region Auvergne' and CEA, France;

German BMBF and the Helmholtz Association;

General Secretariat for Research and Technology, Ministry of Development, Greece;

Hungarian OTKA and National Office for Research and Technology (NKTH);

Department of Atomic Energy and Department of Science and Technology of the Government of India;

Istituto Nazionale di Fisica Nucleare (INFN) of Italy;

MEXT Grant-in-Aid for Specially Promoted Research, Japan;

Joint Institute for Nuclear Research, Dubna;

National Research Foundation of Korea (NRF);

CONACYT, DGAPA, México, ALFA-EC and the HELEN Program (High-Energy physics Latin-American-European Network);

Stichting voor Fundamenteel Onderzoek der Materie (FOM) and the Nederlandse Organisatie voor Wetenschappelijk Onderzoek (NWO), Netherlands;

Research Council of Norway (NFR);

Polish Ministry of Science and Higher Education;

National Authority for Scientific Research - NASR (Autoritatea Națională pentru Cercetare Științifică - ANCS);

Federal Agency of Science of the Ministry of Education and Science of Russian Federation, International Science and Technology Center, Russian Academy of Sciences, Russian Federal Agency of Atomic Energy, Russian Federal Agency for Science and Innovations and CERN-INTAS;

Ministry of Education of Slovakia;

Department of Science and Technology, South Africa;

CIEMAT, EELA, Ministerio de Educación y Ciencia of Spain, Xunta de Galicia (Consellería de Educación), CEADEN, Cubaenergía, Cuba, and IAEA (International Atomic Energy Agency);
Swedish Research Council (VR) and Knut & Alice Wallenberg Foundation (KAW);
Ukraine Ministry of Education and Science;
United Kingdom Science and Technology Facilities Council (STFC);
The United States Department of Energy, the United States National Science Foundation, the State of Texas, and the State of Ohio.

A The ALICE Collaboration

B. Abelev⁶⁸, J. Adam³³, D. Adamová⁷³, A.M. Adare¹²⁰, M.M. Aggarwal⁷⁷, G. Aglieri Rinella²⁹, A.G. Agocs⁶⁰, A. Agostinelli²¹, S. Aguilar Salazar⁵⁶, Z. Ahammed¹¹⁶, N. Ahmad¹³, A. Ahmad Masoodi¹³, S.U. Ahn^{63,36}, A. Akindinov⁴⁶, D. Aleksandrov⁸⁸, B. Alessandro⁹⁴, R. Alfaro Molina⁵⁶, A. Alici^{97,9}, A. Alkin², E. Almaráz Aviña⁵⁶, J. Alme³¹, T. Alt³⁵, V. Altini²⁷, S. Altinpinar¹⁴, I. Altsybeev¹¹⁷, C. Andrei⁷⁰, A. Andronic⁸⁵, V. Anguelov⁸², J. Anielski⁵⁴, C. Anson¹⁵, T. Antičić⁸⁶, F. Antinori⁹³, P. Antonioli⁹⁷, L. Aphecetche¹⁰², H. Appelshäuser⁵², N. Arbor⁶⁴, S. Arcelli²¹, A. Arend⁵², N. Armesto¹², R. Arnaldi⁹⁴, T. Aronsson¹²⁰, I.C. Arsene⁸⁵, M. Arslandok⁵², A. Asryan¹¹⁷, A. Augustinus²⁹, R. Averbeck⁸⁵, T.C. Awes⁷⁴, J. Äystö³⁷, M.D. Azmi¹³, M. Bach³⁵, A. Badalá⁹⁹, Y.W. Baek^{63,36}, R. Bailhache⁵², R. Bala⁹⁴, R. Baldini Ferroli⁹, A. Baldisseri¹¹, A. Baldit⁶³, F. Baltasar Dos Santos Pedrosa²⁹, J. Bán⁴⁷, R.C. Baral⁴⁸, R. Barbera²³, F. Barile²⁷, G.G. Barnaföldi⁶⁰, L.S. Barnby⁹⁰, V. Barret⁶³, J. Bartke¹⁰⁴, M. Basile²¹, N. Bastid⁶³, S. Basu¹¹⁶, B. Bathen⁵⁴, G. Batigne¹⁰², B. Batyunya⁵⁹, C. Baumann⁵², I.G. Bearden⁷¹, H. Beck⁵², I. Belikov⁵⁸, F. Bellini²¹, R. Bellwied¹¹⁰, E. Belmont-Moreno⁵⁶, G. Bencedi⁶⁰, S. Beole²⁵, I. Berceanu⁷⁰, A. Bercuci⁷⁰, Y. Berdnikov⁷⁵, D. Berenyi⁶⁰, D. Berzano⁹⁴, L. Betev²⁹, A. Bhasin⁸⁰, A.K. Bhati⁷⁷, J. Bhowmik¹¹⁴, N. Bianchi⁶⁵, L. Bianchi²⁵, C. Bianchin¹⁹, J. Bielčák³³, J. Bielčíková⁷³, A. Bilandžić^{72,71}, S. Bjelogrić⁴⁵, F. Blanco⁷, F. Blanco¹¹⁰, D. Blau⁸⁸, C. Blume⁵², M. Boccioni²⁹, N. Bock¹⁵, A. Bogdanov⁶⁹, H. Bøggild⁷¹, M. Bogolyubsky⁴³, L. Boldizsár⁶⁰, M. Bombara³⁴, J. Book⁵², H. Borel¹¹, A. Borissov¹¹⁹, S. Bose⁸⁹, F. Bossu²⁵, M. Botje⁷², S. Böttger⁵¹, B. Boyer⁴², E. Braidot⁶⁷, P. Braun-Munzinger⁸⁵, M. Bregant¹⁰², T. Breitner⁵¹, T.A. Browning⁸³, M. Broz³², R. Brun²⁹, E. Bruna^{25,94}, G.E. Bruno²⁷, D. Budnikov⁸⁷, H. Buesching⁵², S. Bufalino^{25,94}, K. Bugaiev², O. Busch⁸², Z. Buthelezi⁷⁹, D. Caballero Orduna¹²⁰, D. Caffarri¹⁹, X. Cai³⁹, H. Caines¹²⁰, E. Calvo Villar⁹¹, P. Camerini²⁰, V. Canoa Roman^{8,1}, G. Cara Romeo⁹⁷, W. Carena²⁹, F. Carena²⁹, N. Carlin Filho¹⁰⁷, F. Carminati²⁹, C.A. Carrillo Montoya²⁹, A. Casanova Díaz⁶⁵, J. Castillo Castellanos¹¹, J.F. Castillo Hernandez⁸⁵, E.A.R. Casula¹⁸, V. Catanesu⁷⁰, C. Cavicchioli²⁹, C. Ceballos Sanchez⁶, J. Cepila³³, P. Cerello⁹⁴, B. Chang^{37,123}, S. Chapeland²⁹, J.L. Charvet¹¹, S. Chattopadhyay⁸⁹, S. Chattopadhyay¹¹⁶, I. Chawla⁷⁷, M. Cherney⁷⁶, C. Cheshkov^{29,109}, B. Cheynis¹⁰⁹, V. Chibante Barroso²⁹, D.D. Chinellato¹⁰⁸, P. Chochula²⁹, M. Chojnacki⁴⁵, S. Choudhury¹¹⁶, P. Christakoglou^{72,45}, C.H. Christensen⁷¹, P. Christiansen²⁸, T. Chujo¹¹⁴, S.U. Chung⁸⁴, C. Cicalo⁹⁶, L. Cifarelli^{21,29}, F. Cindolo⁹⁷, J. Cleymans⁷⁹, F. Coccetti⁹, F. Colamaria²⁷, D. Colella²⁷, G. Conesa Balbastre⁶⁴, Z. Conesa del Valle²⁹, P. Constantin⁸², G. Contin²⁰, J.G. Contreras⁸, T.M. Cormier¹¹⁹, Y. Corrales Morales²⁵, P. Cortese²⁶, I. Cortés Maldonado¹, M.R. Cosentino^{67,108}, F. Costa²⁹, M.E. Cotallo⁷, E. Crescio⁸, P. Crochet⁶³, E. Cruz Alaniz⁵⁶, E. Cuautle⁵⁵, L. Cunqueiro⁶⁵, A. Dainese^{19,93}, H.H. Dalsgaard⁷¹, A. Danu⁵⁰, K. Das⁸⁹, I. Das^{89,42}, D. Das⁸⁹, A. Dash¹⁰⁸, S. Dash⁴⁰, S. De¹¹⁶, G.O.V. de Barros¹⁰⁷, A. De Caro^{24,9}, G. de Cataldo⁹⁸, J. de Cuveland³⁵, A. De Falco¹⁸, D. De Gruttola²⁴, H. Delagrangé¹⁰², E. Del Castillo Sanchez²⁹, A. Deloff¹⁰⁰, V. Demanov⁸⁷, N. De Marco⁹⁴, E. Dénes⁶⁰, S. De Pasquale²⁴, A. Deppman¹⁰⁷, G. D'Erasmus²⁷, R. de Rooij⁴⁵, M.A. Diaz Corchero⁷, D. Di Bari²⁷, T. Dietel⁵⁴, C. Di Giglio²⁷, S. Di Liberto⁹⁵, A. Di Mauro²⁹, P. Di Nezza⁶⁵, R. Divià²⁹, Ø. Djuvsland¹⁴, A. Dobrin^{119,28}, T. Dobrowolski¹⁰⁰, I. Domínguez⁵⁵, B. Dönigus⁸⁵, O. Dordic¹⁷, O. Driga¹⁰², A.K. Dubey¹¹⁶, L. Ducroux¹⁰⁹, P. Dupieux⁶³, A.K. Dutta Majumdar⁸⁹, M.R. Dutta Majumdar¹¹⁶, D. Elia⁹⁸, D. Emschermann⁵⁴, H. Engel⁵¹, H.A. Erdal³¹, B. Espagnon⁴², M. Estienne¹⁰², S. Esumi¹¹⁴, D. Evans⁹⁰, G. Eyyubova¹⁷, D. Fabris^{19,93}, J. Faivre⁶⁴, D. Falchieri²¹, A. Fantoni⁶⁵, M. Fasel⁸⁵, R. Fearick⁷⁹, A. Fedunov⁵⁹, D. Fehlfker¹⁴, L. Feldkamp⁵⁴, D. Felea⁵⁰, B. Fenton-Olsen⁶⁷, G. Feofilov¹¹⁷, A. Fernández Téllez¹, A. Ferretti²⁵, R. Ferretti²⁶, J. Figiel¹⁰⁴, M.A.S. Figueredo¹⁰⁷, S. Filchagin⁸⁷, D. Finogeev⁴⁴, F.M. Fionda²⁷, E.M. Fiore²⁷, M. Floris²⁹, S. Foertsch⁷⁹, P. Foka⁸⁵, S. Fokin⁸⁸, E. Fragiaco⁹², M. Fragkiadakis⁷⁸, U. Frankenfeld⁸⁵, U. Fuchs²⁹, C. Furget⁶⁴, M. Fusco Girard²⁴, J.J. Gaardhøje⁷¹, M. Gagliardi²⁵, A. Gago⁹¹, M. Gallio²⁵, D.R. Gangadharan¹⁵, P. Ganoti⁷⁴, C. Garabatos⁸⁵, E. Garcia-Solis¹⁰, I. Garishvili⁶⁸, J. Gerhard³⁵, M. Germain¹⁰², C. Geuna¹¹, M. Gheata²⁹, A. Gheata²⁹, B. Ghidini²⁷, P. Ghosh¹¹⁶, P. Gianotti⁶⁵, M.R. Girard¹¹⁸, P. Giubellino²⁹, E. Gladysz-Dziadus¹⁰⁴, P. Glässel⁸², R. Gomez¹⁰⁶, E.G. Ferreira¹², L.H. González-Trueba⁵⁶, P. González-Zamora⁷, S. Gorbunov³⁵, A. Goswami⁸¹, S. Gotovac¹⁰³, V. Grabski⁵⁶, L.K. Graczykowski¹¹⁸, R. Gracjarek⁸², A. Grelli⁴⁵, C. Grigoras²⁹, A. Grigoras²⁹, V. Grigoriev⁶⁹, S. Grigoryan⁵⁹, A. Grigoryan¹²¹, B. Grinyov², N. Grion⁹², P. Gros²⁸, J.F. Grosse-Oetringhaus²⁹, J.-Y. Grossiord¹⁰⁹, R. Grosso²⁹, F. Guber⁴⁴, R. Guernane⁶⁴, C. Guerra Gutierrez⁹¹, B. Guerzoni²¹, M. Guilbaud¹⁰⁹, K. Gulbrandsen⁷¹, T. Gunji¹¹³, R. Gupta⁸⁰, A. Gupta⁸⁰, H. Gutbrod⁸⁵, Ø. Haaland¹⁴, C. Hadjidakis⁴², M. Haiduc⁵⁰, H. Hamagaki¹¹³, G. Hamar⁶⁰, B.H. Han¹⁶, L.D. Hanratty⁹⁰, A. Hansen⁷¹, Z. Harmanova³⁴, J.W. Harris¹²⁰, M. Hartig⁵², D. Hasegan⁵⁰, D. Hatzifotiadou⁹⁷, A. Hayrapetyan^{29,121}, S.T. Heckel⁵², M. Heide⁵⁴, H. Helstrup³¹, A. Hergelegiu⁷⁰, G. Herrera Corral⁸, N. Herrmann⁸², K.F. Hetland³¹, B. Hicks¹²⁰, P.T. Hille¹²⁰, B. Hippolyte⁵⁸, T. Horaguchi¹¹⁴, Y. Hori¹¹³,

P. Hristov²⁹, I. Hřivnáčová⁴², M. Huang¹⁴, T.J. Humanic¹⁵, D.S. Hwang¹⁶, R. Ichou⁶³, R. Ilkaev⁸⁷, I. Ilkiv¹⁰⁰, M. Inaba¹¹⁴, E. Incani¹⁸, P.G. Innocenti²⁹, G.M. Innocenti²⁵, M. Ippolitov⁸⁸, M. Irfan¹³, C. Ivan⁸⁵, V. Ivanov⁷⁵, A. Ivanov¹¹⁷, M. Ivanov⁸⁵, O. Ivanytskyi², A. Jachoňkowski²⁹, P. M. Jacobs⁶⁷, L. Jancurová⁵⁹, H.J. Jang⁶², S. Jangal⁵⁸, R. Janik³², M.A. Janik¹¹⁸, P.H.S.Y. Jayarathna¹¹⁰, S. Jena⁴⁰, D.M. Jha¹¹⁹, R.T. Jimenez Bustamante⁵⁵, L. Jirden²⁹, P.G. Jones⁹⁰, H. Jung³⁶, A. Jusko⁹⁰, A.B. Kaidalov⁴⁶, V. Kakoyan¹²¹, S. Kalcher³⁵, P. Kaliňák⁴⁷, M. Kalisky⁵⁴, T. Kalliokoski³⁷, A. Kalweit⁵³, K. Kanaki¹⁴, J.H. Kang¹²³, V. Kaplin⁶⁹, A. Karasu Uysal^{29,122}, O. Karavichev⁴⁴, T. Karavicheva⁴⁴, E. Karpechev⁴⁴, A. Kazantsev⁸⁸, U. Keschull⁵¹, R. Keidel¹²⁴, M.M. Khan¹³, S.A. Khan¹¹⁶, A. Khanzadeev⁷⁵, Y. Kharlov⁴³, B. Kileng³¹, J.S. Kim³⁶, D.W. Kim³⁶, S.H. Kim³⁶, J.H. Kim¹⁶, M. Kim¹²³, D.J. Kim³⁷, B. Kim¹²³, T. Kim¹²³, S. Kim¹⁶, S. Kirsch³⁵, I. Kisel³⁵, S. Kiselev⁴⁶, A. Kisiel^{29,118}, J.L. Klay⁴, J. Klein⁸², C. Klein-Bösing⁵⁴, M. Kliemant⁵², A. Kluge²⁹, M.L. Knichel⁸⁵, A.G. Knospe¹⁰⁵, K. Koch⁸², M.K. Köhler⁸⁵, A. Kolojvari¹¹⁷, V. Kondratiev¹¹⁷, N. Kondratyeva⁶⁹, A. Konevskikh⁴⁴, A. Korneev⁸⁷, R. Kour⁹⁰, M. Kowalski¹⁰⁴, S. Kox⁶⁴, G. Koyithatta Meethalevedu⁴⁰, J. Kral³⁷, I. Králik⁴⁷, F. Kramer⁵², I. Kraus⁸⁵, T. Krawutschke^{82,30}, M. Krelina³³, M. Kretz³⁵, M. Krivda^{90,47}, F. Krizek³⁷, M. Krus³³, E. Kryshen⁷⁵, M. Krzewicki^{72,85}, Y. Kucheriaev⁸⁸, C. Kuhn⁵⁸, P.G. Kuijer⁷², P. Kurashvili¹⁰⁰, A. Kurepin⁴⁴, A.B. Kurepin⁴⁴, A. Kuryakin⁸⁷, V. Kuschpil⁷³, S. Kuschpil⁷³, H. Kvaerno¹⁷, M.J. Kweon⁸², Y. Kwon¹²³, P. Ladrón de Guevara⁵⁵, I. Lakomov^{42,117}, R. Langoy¹⁴, S.L. La Pointe⁴⁵, C. Lara⁵¹, A. Lardeux¹⁰², P. La Rocca²³, C. Lazzeroni⁹⁰, R. Lea²⁰, Y. Le Bornec⁴², M. Lechman²⁹, S.C. Lee³⁶, K.S. Lee³⁶, F. Lefèvre¹⁰², J. Lehnert⁵², L. Leistam²⁹, M. Lenhardt¹⁰², V. Lenti⁹⁸, H. León⁵⁶, I. León Monzón¹⁰⁶, H. León Vargas⁵², P. Léval⁶⁰, J. Lien¹⁴, R. Lietava⁹⁰, S. Lindal¹⁷, V. Lindenstruth³⁵, C. Lippmann^{85,29}, M.A. Lisa¹⁵, L. Liu¹⁴, P.I. Loenne¹⁴, V.R. Loggins¹¹⁹, V. Loginov⁶⁹, S. Lohn²⁹, D. Lohner⁸², C. Loizides⁶⁷, K.K. Loo³⁷, X. Lopez⁶³, E. López Torres⁶, G. Løvnhøiden¹⁷, X.-G. Lu⁸², P. Luettig⁵², M. Lunardon¹⁹, J. Luo³⁹, G. Luparello⁴⁵, L. Luquin¹⁰², C. Luzzi²⁹, R. Ma¹²⁰, K. Ma³⁹, D.M. Madagodahettige-Don¹¹⁰, A. Maevskaya⁴⁴, M. Mager^{53,29}, D.P. Mahapatra⁴⁸, A. Maire⁵⁸, M. Malaev⁷⁵, I. Maldonado Cervantes⁵⁵, L. Malinina^{59,ii}, D. Mal'Kevich⁴⁶, P. Malzacher⁸⁵, A. Mamonov⁸⁷, L. Manceau⁹⁴, L. Mangotra⁸⁰, V. Manko⁸⁸, F. Manso⁶³, V. Manzarí⁹⁸, Y. Mao^{64,39}, M. Marchisone^{63,25}, J. Mareš⁴⁹, G.V. Margagliotti^{20,92}, A. Margotti⁹⁷, A. Marín⁸⁵, C.A. Marin Tobon²⁹, C. Markert¹⁰⁵, I. Martashvili¹¹², P. Martinengo²⁹, M.I. Martínez¹, A. Martínez Davalos⁵⁶, G. Martínez García¹⁰², Y. Martynov², A. Mas¹⁰², S. Masciocchi⁸⁵, M. Maserà²⁵, A. Masoni⁹⁶, L. Massacrier^{109,102}, M. Mastromarco⁹⁸, A. Mastroserio^{27,29}, Z.L. Matthews⁹⁰, A. Matyjka^{104,102}, D. Mayani⁵⁵, C. Mayer¹⁰⁴, J. Mazer¹¹², M.A. Mazzoni⁹⁵, F. Meddi²², A. Menchaca-Rocha⁵⁶, J. Mercado Pérez⁸², M. Meres³², Y. Miake¹¹⁴, L. Milano²⁵, J. Milosevic^{17,iii}, A. Mischke⁴⁵, A.N. Mishra⁸¹, D. Miśkowiec^{85,29}, C. Mitu⁵⁰, J. Mlynarz¹¹⁹, A.K. Mohanty²⁹, B. Mohanty¹¹⁶, L. Molnar²⁹, L. Montaño Zetina⁸, M. Monteno⁹⁴, E. Montes⁷, T. Moon¹²³, M. Morando¹⁹, D.A. Moreira De Godoy¹⁰⁷, S. Moretto¹⁹, A. Morsch²⁹, V. Muccifora⁶⁵, E. Mudnic¹⁰³, S. Muhuri¹¹⁶, M. Mukherjee¹¹⁶, H. Müller²⁹, M.G. Munhoz¹⁰⁷, L. Musa²⁹, A. Musso⁹⁴, B.K. Nandi⁴⁰, R. Nania⁹⁷, E. Nappi⁹⁸, C. Nattrass¹¹², N.P. Naumov⁸⁷, S. Navin⁹⁰, T.K. Nayak¹¹⁶, S. Nazarenko⁸⁷, G. Nazarov⁸⁷, A. Nedosekin⁴⁶, M. Nicassio²⁷, B.S. Nielsen⁷¹, T. Niida¹¹⁴, S. Nikolaev⁸⁸, V. Nikolic⁸⁶, V. Nikulin⁷⁵, S. Nikulin⁸⁸, B.S. Nilsen⁷⁶, M.S. Nilsson¹⁷, F. Noferini^{97,9}, P. Nomokonov⁵⁹, G. Nooren⁴⁵, N. Novitzky³⁷, A. Nyman⁸⁸, A. Nyatha⁴⁰, C. Nygaard⁷¹, J. Nystrand¹⁴, A. Ochirov¹¹⁷, H. Oeschler^{53,29}, S. Oh¹²⁰, S.K. Oh³⁶, J. Oleniacz¹¹⁸, C. Oppedisano⁹⁴, A. Ortiz Velasquez^{28,55}, G. Ortona²⁵, A. Oskarsson²⁸, P. Ostrowski¹¹⁸, J. Otwinowski⁸⁵, K. Oyama⁸², K. Ozawa¹¹³, Y. Pachmayer⁸², M. Pachr³³, F. Padilla²⁵, P. Pagano²⁴, G. Paic⁵⁵, F. Painke³⁵, C. Pajares¹², S.K. Pal¹¹⁶, S. Pal¹¹, A. Palaha⁹⁰, A. Palmeri⁹⁹, V. Papikyan¹²¹, G.S. Pappalardo⁹⁹, W.J. Park⁸⁵, A. Passfeld⁵⁴, B. Pastirčák⁴⁷, D.I. Patalakha⁴³, V. Paticchio⁹⁸, A. Pavlinov¹¹⁹, T. Pawlak¹¹⁸, T. Peitzmann⁴⁵, H. Pereira Da Costa¹¹, E. Pereira De Oliveira Filho¹⁰⁷, D. Peresunko⁸⁸, C.E. Pérez Lara⁷², E. Perez Lezama⁵⁵, D. Perini²⁹, D. Perrino²⁷, W. Peryt¹¹⁸, A. Pesci⁹⁷, V. Peskov^{29,55}, Y. Pestov³, V. Petráček³³, M. Petran³³, M. Petris⁷⁰, P. Petrov⁹⁰, M. Petrovici⁷⁰, C. Petta²³, S. Piano⁹², A. Piccotti⁹⁴, M. Pikna³², P. Pillot¹⁰², O. Pinazza²⁹, L. Pinsky¹¹⁰, N. Pitz⁵², D.B. Piyarathna¹¹⁰, M. Płoskoń⁶⁷, J. Pluta¹¹⁸, T. Pocheptsov⁵⁹, S. Pochybova⁶⁰, P.L.M. Podesta-Lerma¹⁰⁶, M.G. Poghosyan^{29,25}, K. Polák⁴⁹, B. Polichtchouk⁴³, A. Pop⁷⁰, S. Porteboeuf-Houssais⁶³, V. Pospíšil³³, B. Potukuchi⁸⁰, S.K. Prasad¹¹⁹, R. Preghenella^{97,9}, F. Prino⁹⁴, C.A. Pruneau¹¹⁹, I. Pshenichnov⁴⁴, S. Puchagin⁸⁷, G. Puudu¹⁸, J. Pujol Teixido⁵¹, A. Pulvirenti^{23,29}, V. Punin⁸⁷, M. Putiš³⁴, J. Putschke^{119,120}, E. Quercigh²⁹, H. Qvigstad¹⁷, A. Rachevski⁹², A. Rademakers²⁹, S. Radomski⁸², T.S. Rähä³⁷, J. Rak³⁷, A. Rakotozafindrabe¹¹, L. Ramello²⁶, A. Ramírez Reyes⁸, R. Raniwala⁸¹, S. Raniwala⁸¹, S.S. Räsänen³⁷, B.T. Rascanu⁵², D. Rathee⁷⁷, K.F. Read¹¹², J.S. Real⁶⁴, K. Redlich^{100,57}, P. Reichelt⁵², M. Reicher⁴⁵, R. Renfordt⁵², A.R. Reolon⁶⁵, A. Reshetin⁴⁴, F. Rettig³⁵, J.-P. Revol²⁹, K. Reygers⁸², L. Riccati⁹⁴, R.A. Ricci⁶⁶, T. Richert²⁸, M. Richter¹⁷, P. Riedler²⁹, W. Riegler²⁹, F. Riggi^{23,99}, B. Rodrigues Fernandes Rabacal²⁹,

M. Rodríguez Cahuantzi¹, A. Rodriguez Manso⁷², K. Røed¹⁴, D. Rohr³⁵, D. Röhrich¹⁴, R. Romita⁸⁵, F. Ronchetti⁶⁵, P. Rosnet⁶³, S. Rossegger²⁹, A. Rossi¹⁹, F. Roukoutakis⁷⁸, P. Roy⁸⁹, C. Roy⁵⁸, A.J. Rubio Montero⁷, R. Rui²⁰, E. Ryabinkin⁸⁸, A. Rybicki¹⁰⁴, S. Sadovsky⁴³, K. Šafařík²⁹, R. Sahoo⁴¹, P.K. Sahu⁴⁸, J. Saini¹¹⁶, H. Sakaguchi³⁸, S. Sakai⁶⁷, D. Sakata¹¹⁴, C.A. Salgado¹², J. Salzwedel¹⁵, S. Sambyal⁸⁰, V. Samsonov⁷⁵, X. Sanchez Castro^{55,58}, L. Šándor⁴⁷, A. Sandoval⁵⁶, S. Sano¹¹³, M. Sano¹¹⁴, R. Santo⁵⁴, R. Santoro^{98,29}, J. Sarkamo³⁷, E. Scapparone⁹⁷, F. Scarlassara¹⁹, R.P. Scharenberg⁸³, C. Schiaua⁷⁰, R. Schicker⁸², C. Schmidt⁸⁵, H.R. Schmidt^{85,115}, S. Schreiner²⁹, S. Schuchmann⁵², J. Schukraft²⁹, Y. Schutz^{29,102}, K. Schwarz⁸⁵, K. Schweda^{85,82}, G. Scioli²¹, E. Scomparin⁹⁴, R. Scott¹¹², P.A. Scott⁹⁰, G. Segato¹⁹, I. Selyuzhenkov⁸⁵, S. Senyukov^{26,58}, J. Seo⁸⁴, S. Serçi¹⁸, E. Serradilla^{7,56}, A. Sevcenco⁵⁰, I. Sgura⁹⁸, A. Shabetai¹⁰², G. Shabratova⁵⁹, R. Shahoyan²⁹, N. Sharma⁷⁷, S. Sharma⁸⁰, K. Shigaki³⁸, M. Shimomura¹¹⁴, K. Shtejer⁶, Y. Sibiriak⁸⁸, M. Siciliano²⁵, E. Sicking²⁹, S. Siddhanta⁹⁶, T. Siemiarczuk¹⁰⁰, D. Silvermyr⁷⁴, c. Silvestre⁶⁴, G. Simonetti^{27,29}, R. Singaraju¹¹⁶, R. Singh⁸⁰, S. Singha¹¹⁶, B.C. Sinha¹¹⁶, T. Sinha⁸⁹, B. Sitar³², M. Sitta²⁶, T.B. Skaali¹⁷, K. Skjerdal¹⁴, R. Smakal³³, N. Smirnov¹²⁰, R.J.M. Snellings⁴⁵, C. Sogaard⁷¹, R. Soltz⁶⁸, H. Son¹⁶, M. Song¹²³, J. Song⁸⁴, C. Soos²⁹, F. Soramel¹⁹, I. Sputowska¹⁰⁴, M. Spyropoulou-Stassinaki⁷⁸, B.K. Srivastava⁸³, J. Stachel⁸², I. Stan⁵⁰, I. Stan⁵⁰, G. Stefanek¹⁰⁰, T. Steinbeck³⁵, M. Steinpreis¹⁵, E. Stenlund²⁸, G. Steyn⁷⁹, J.H. Stiller⁸², D. Stocco¹⁰², M. Stolpovskiy⁴³, K. Strabykin⁸⁷, P. Strmen³², A.A.P. Suaide¹⁰⁷, M.A. Subieta Vásquez²⁵, T. Sugitate³⁸, C. Suire⁴², M. Sukhorukov⁸⁷, R. Sultanov⁴⁶, M. Šumbera⁷³, T. Susa⁸⁶, A. Szanto de Toledo¹⁰⁷, I. Szarka³², A. Szostak¹⁴, C. Tagridis⁷⁸, J. Takahashi¹⁰⁸, J.D. Tapia Takaki⁴², A. Tauro²⁹, G. Tejada Muñoz¹, A. Telesca²⁹, C. Terrevoli²⁷, J. Thäder⁸⁵, D. Thomas⁴⁵, R. Tieulent¹⁰⁹, A.R. Timmins¹¹⁰, D. Tlusty³³, A. Toia^{35,29}, H. Torii^{38,113}, L. Toscano⁹⁴, D. Truesdale¹⁵, W.H. Trzaska³⁷, T. Tsuji¹¹³, A. Tumkin⁸⁷, R. Turrisi⁹³, T.S. Tveter¹⁷, J. Ulery⁵², K. Ullaland¹⁴, J. Ulrich^{61,51}, A. Uras¹⁰⁹, J. Urbán³⁴, G.M. Urciuoli⁹⁵, G.L. Usai¹⁸, M. Vajzer^{33,73}, M. Vala^{59,47}, L. Valencia Palomo⁴², S. Vallero⁸², N. van der Kolk⁷², P. Vande Vyve²⁹, M. van Leeuwen⁴⁵, L. Vannucci⁶⁶, A. Vargas¹, R. Varma⁴⁰, M. Vasileiou⁷⁸, A. Vasiliev⁸⁸, V. Vechernin¹¹⁷, M. Veldhoen⁴⁵, M. Venaruzzo²⁰, E. Vercellin²⁵, S. Vergara¹, R. Vernet⁵, M. Verweij⁴⁵, L. Vickovic¹⁰³, G. Viesti¹⁹, O. Vikhlyantsev⁸⁷, Z. Vilakazi⁷⁹, O. Villalobos Baillie⁹⁰, A. Vinogradov⁸⁸, L. Vinogradov¹¹⁷, Y. Vinogradov⁸⁷, T. Virgili²⁴, Y.P. Viyogi¹¹⁶, A. Vodopyanov⁵⁹, S. Voloshin¹¹⁹, K. Voloshin⁴⁶, G. Volpe^{27,29}, B. von Haller²⁹, D. Vranic⁸⁵, G. Øvrebekk¹⁴, J. Vrláková³⁴, B. Vulpescu⁶³, A. Vyushin⁸⁷, B. Wagner¹⁴, V. Wagner³³, R. Wan^{58,39}, Y. Wang⁸², D. Wang³⁹, Y. Wang³⁹, M. Wang³⁹, K. Watanabe¹¹⁴, J.P. Wessels^{29,54}, U. Westerhoff⁵⁴, J. Wiechula¹¹⁵, J. Wikne¹⁷, M. Wilde⁵⁴, G. Wilk¹⁰⁰, A. Wilk⁵⁴, M.C.S. Williams⁹⁷, B. Windelband⁸², L. Xaplanteris Karampatsos¹⁰⁵, C.G. Yaldo¹¹⁹, H. Yang¹¹, S. Yang¹⁴, S. Yasnopolskiy⁸⁸, J. Yi⁸⁴, Z. Yin³⁹, I.-K. Yoo⁸⁴, J. Yoon¹²³, W. Yu⁵², X. Yuan³⁹, I. Yushmanov⁸⁸, C. Zach³³, C. Zampolli⁹⁷, S. Zaporozhets⁵⁹, A. Zarochentsev¹¹⁷, P. Závada⁴⁹, N. Zaviyalov⁸⁷, H. Zbroszczyk¹¹⁸, P. Zelnicsek⁵¹, I.S. Zgura⁵⁰, M. Zhalov⁷⁵, H. Zhang³⁹, X. Zhang^{63,39}, D. Zhou³⁹, F. Zhou³⁹, Y. Zhou⁴⁵, X. Zhu³⁹, J. Zhu³⁹, J. Zhu³⁹, A. Zichichi^{21,9}, A. Zimmermann⁸², G. Zinovjev², Y. Zoccarato¹⁰⁹, M. Zynovyev²

Affiliation notes

- ⁱ Also at: M.V.Lomonosov Moscow State University, D.V.Skobeltzyn Institute of Nuclear Physics, Moscow, Russia
ⁱⁱ Also at: "Vinča" Institute of Nuclear Sciences, Belgrade, Serbia

Collaboration Institutes

- ¹ Benemérita Universidad Autónoma de Puebla, Puebla, Mexico
- ² Bogolyubov Institute for Theoretical Physics, Kiev, Ukraine
- ³ Budker Institute for Nuclear Physics, Novosibirsk, Russia
- ⁴ California Polytechnic State University, San Luis Obispo, California, United States
- ⁵ Centre de Calcul de l'IN2P3, Villeurbanne, France
- ⁶ Centro de Aplicaciones Tecnológicas y Desarrollo Nuclear (CEADEN), Havana, Cuba
- ⁷ Centro de Investigaciones Energéticas Medioambientales y Tecnológicas (CIEMAT), Madrid, Spain
- ⁸ Centro de Investigación y de Estudios Avanzados (CINVESTAV), Mexico City and Mérida, Mexico
- ⁹ Centro Fermi – Centro Studi e Ricerche e Museo Storico della Fisica "Enrico Fermi", Rome, Italy
- ¹⁰ Chicago State University, Chicago, United States
- ¹¹ Commissariat à l'Énergie Atomique, IRFU, Saclay, France
- ¹² Departamento de Física de Partículas and IGFAE, Universidad de Santiago de Compostela, Santiago de Compostela, Spain

- 13 Department of Physics Aligarh Muslim University, Aligarh, India
- 14 Department of Physics and Technology, University of Bergen, Bergen, Norway
- 15 Department of Physics, Ohio State University, Columbus, Ohio, United States
- 16 Department of Physics, Sejong University, Seoul, South Korea
- 17 Department of Physics, University of Oslo, Oslo, Norway
- 18 Dipartimento di Fisica dell'Università and Sezione INFN, Cagliari, Italy
- 19 Dipartimento di Fisica dell'Università and Sezione INFN, Padova, Italy
- 20 Dipartimento di Fisica dell'Università and Sezione INFN, Trieste, Italy
- 21 Dipartimento di Fisica dell'Università and Sezione INFN, Bologna, Italy
- 22 Dipartimento di Fisica dell'Università 'La Sapienza' and Sezione INFN, Rome, Italy
- 23 Dipartimento di Fisica e Astronomia dell'Università and Sezione INFN, Catania, Italy
- 24 Dipartimento di Fisica 'E.R. Caianiello' dell'Università and Gruppo Collegato INFN, Salerno, Italy
- 25 Dipartimento di Fisica Sperimentale dell'Università and Sezione INFN, Turin, Italy
- 26 Dipartimento di Scienze e Tecnologie Avanzate dell'Università del Piemonte Orientale and Gruppo Collegato INFN, Alessandria, Italy
- 27 Dipartimento Interateneo di Fisica 'M. Merlin' and Sezione INFN, Bari, Italy
- 28 Division of Experimental High Energy Physics, University of Lund, Lund, Sweden
- 29 European Organization for Nuclear Research (CERN), Geneva, Switzerland
- 30 Fachhochschule Köln, Köln, Germany
- 31 Faculty of Engineering, Bergen University College, Bergen, Norway
- 32 Faculty of Mathematics, Physics and Informatics, Comenius University, Bratislava, Slovakia
- 33 Faculty of Nuclear Sciences and Physical Engineering, Czech Technical University in Prague, Prague, Czech Republic
- 34 Faculty of Science, P.J. Šafárik University, Košice, Slovakia
- 35 Frankfurt Institute for Advanced Studies, Johann Wolfgang Goethe-Universität Frankfurt, Frankfurt, Germany
- 36 Gangneung-Wonju National University, Gangneung, South Korea
- 37 Helsinki Institute of Physics (HIP) and University of Jyväskylä, Jyväskylä, Finland
- 38 Hiroshima University, Hiroshima, Japan
- 39 Hua-Zhong Normal University, Wuhan, China
- 40 Indian Institute of Technology, Mumbai, India
- 41 Indian Institute of Technology Indore (IIT), Indore, India
- 42 Institut de Physique Nucléaire d'Orsay (IPNO), Université Paris-Sud, CNRS-IN2P3, Orsay, France
- 43 Institute for High Energy Physics, Protvino, Russia
- 44 Institute for Nuclear Research, Academy of Sciences, Moscow, Russia
- 45 Nikhef, National Institute for Subatomic Physics and Institute for Subatomic Physics of Utrecht University, Utrecht, Netherlands
- 46 Institute for Theoretical and Experimental Physics, Moscow, Russia
- 47 Institute of Experimental Physics, Slovak Academy of Sciences, Košice, Slovakia
- 48 Institute of Physics, Bhubaneswar, India
- 49 Institute of Physics, Academy of Sciences of the Czech Republic, Prague, Czech Republic
- 50 Institute of Space Sciences (ISS), Bucharest, Romania
- 51 Institut für Informatik, Johann Wolfgang Goethe-Universität Frankfurt, Frankfurt, Germany
- 52 Institut für Kernphysik, Johann Wolfgang Goethe-Universität Frankfurt, Frankfurt, Germany
- 53 Institut für Kernphysik, Technische Universität Darmstadt, Darmstadt, Germany
- 54 Institut für Kernphysik, Westfälische Wilhelms-Universität Münster, Münster, Germany
- 55 Instituto de Ciencias Nucleares, Universidad Nacional Autónoma de México, Mexico City, Mexico
- 56 Instituto de Física, Universidad Nacional Autónoma de México, Mexico City, Mexico
- 57 Institut of Theoretical Physics, University of Wrocław
- 58 Institut Pluridisciplinaire Hubert Curien (IPHC), Université de Strasbourg, CNRS-IN2P3, Strasbourg, France
- 59 Joint Institute for Nuclear Research (JINR), Dubna, Russia
- 60 KFKI Research Institute for Particle and Nuclear Physics, Hungarian Academy of Sciences, Budapest, Hungary
- 61 Kirchhoff-Institut für Physik, Ruprecht-Karls-Universität Heidelberg, Heidelberg, Germany
- 62 Korea Institute of Science and Technology Information, Daejeon, South Korea

- 63 Laboratoire de Physique Corpusculaire (LPC), Clermont Université, Université Blaise Pascal, CNRS–IN2P3, Clermont-Ferrand, France
- 64 Laboratoire de Physique Subatomique et de Cosmologie (LPSC), Université Joseph Fourier, CNRS-IN2P3, Institut Polytechnique de Grenoble, Grenoble, France
- 65 Laboratori Nazionali di Frascati, INFN, Frascati, Italy
- 66 Laboratori Nazionali di Legnaro, INFN, Legnaro, Italy
- 67 Lawrence Berkeley National Laboratory, Berkeley, California, United States
- 68 Lawrence Livermore National Laboratory, Livermore, California, United States
- 69 Moscow Engineering Physics Institute, Moscow, Russia
- 70 National Institute for Physics and Nuclear Engineering, Bucharest, Romania
- 71 Niels Bohr Institute, University of Copenhagen, Copenhagen, Denmark
- 72 Nikhef, National Institute for Subatomic Physics, Amsterdam, Netherlands
- 73 Nuclear Physics Institute, Academy of Sciences of the Czech Republic, Řež u Prahy, Czech Republic
- 74 Oak Ridge National Laboratory, Oak Ridge, Tennessee, United States
- 75 Petersburg Nuclear Physics Institute, Gatchina, Russia
- 76 Physics Department, Creighton University, Omaha, Nebraska, United States
- 77 Physics Department, Panjab University, Chandigarh, India
- 78 Physics Department, University of Athens, Athens, Greece
- 79 Physics Department, University of Cape Town, iThemba LABS, Cape Town, South Africa
- 80 Physics Department, University of Jammu, Jammu, India
- 81 Physics Department, University of Rajasthan, Jaipur, India
- 82 Physikalisches Institut, Ruprecht-Karls-Universität Heidelberg, Heidelberg, Germany
- 83 Purdue University, West Lafayette, Indiana, United States
- 84 Pusan National University, Pusan, South Korea
- 85 Research Division and ExtreMe Matter Institute EMMI, GSI Helmholtzzentrum für Schwerionenforschung, Darmstadt, Germany
- 86 Rudjer Bošković Institute, Zagreb, Croatia
- 87 Russian Federal Nuclear Center (VNIIEF), Sarov, Russia
- 88 Russian Research Centre Kurchatov Institute, Moscow, Russia
- 89 Saha Institute of Nuclear Physics, Kolkata, India
- 90 School of Physics and Astronomy, University of Birmingham, Birmingham, United Kingdom
- 91 Sección Física, Departamento de Ciencias, Pontificia Universidad Católica del Perú, Lima, Peru
- 92 Sezione INFN, Trieste, Italy
- 93 Sezione INFN, Padova, Italy
- 94 Sezione INFN, Turin, Italy
- 95 Sezione INFN, Rome, Italy
- 96 Sezione INFN, Cagliari, Italy
- 97 Sezione INFN, Bologna, Italy
- 98 Sezione INFN, Bari, Italy
- 99 Sezione INFN, Catania, Italy
- 100 Soltan Institute for Nuclear Studies, Warsaw, Poland
- 101 Nuclear Physics Group, STFC Daresbury Laboratory, Daresbury, United Kingdom
- 102 SUBATECH, Ecole des Mines de Nantes, Université de Nantes, CNRS-IN2P3, Nantes, France
- 103 Technical University of Split FESB, Split, Croatia
- 104 The Henryk Niewodniczanski Institute of Nuclear Physics, Polish Academy of Sciences, Cracow, Poland
- 105 The University of Texas at Austin, Physics Department, Austin, TX, United States
- 106 Universidad Autónoma de Sinaloa, Culiacán, Mexico
- 107 Universidade de São Paulo (USP), São Paulo, Brazil
- 108 Universidade Estadual de Campinas (UNICAMP), Campinas, Brazil
- 109 Université de Lyon, Université Lyon 1, CNRS/IN2P3, IPN-Lyon, Villeurbanne, France
- 110 University of Houston, Houston, Texas, United States
- 111 University of Technology and Austrian Academy of Sciences, Vienna, Austria
- 112 University of Tennessee, Knoxville, Tennessee, United States
- 113 University of Tokyo, Tokyo, Japan
- 114 University of Tsukuba, Tsukuba, Japan
- 115 Eberhard Karls Universität Tübingen, Tübingen, Germany

- ¹¹⁶ Variable Energy Cyclotron Centre, Kolkata, India
- ¹¹⁷ V. Fock Institute for Physics, St. Petersburg State University, St. Petersburg, Russia
- ¹¹⁸ Warsaw University of Technology, Warsaw, Poland
- ¹¹⁹ Wayne State University, Detroit, Michigan, United States
- ¹²⁰ Yale University, New Haven, Connecticut, United States
- ¹²¹ Yerevan Physics Institute, Yerevan, Armenia
- ¹²² Yildiz Technical University, Istanbul, Turkey
- ¹²³ Yonsei University, Seoul, South Korea
- ¹²⁴ Zentrum für Technologietransfer und Telekommunikation (ZTT), Fachhochschule Worms, Worms, Germany